Exploring the ENSO Modulation of the QBO Periods with GISS E2.2 Models

Tiehan Zhou[1,2], Kevin J. DallaSanta[1,3], Clara Orbe[1,3], David H. Rind[1], Jeffrey A. Jonas[1,2], Larissa Nazarenko[1,2], Gavin A. Schmidt[1], Gary Russell[1]

[1]NASA Goddard Institute for Space Studies, New York, NY
[2]Center for Climate Systems Research, Columbia University, New York, NY
[3]Department of Applied Physics and Applied Mathematics, Columbia University, New York, NY

Correspondence to: Tiehan Zhou (tz2131@columbia.edu)

Abstract. Observational studies have shown that the El Niño–Southern Oscillation (ENSO) exerts an influence on the Quasi-Biennial Oscillation (QBO). The downward propagation of the QBO tends to speed up and slow down during El Niño and La Niña, respectively. Recent results from general circulation models have indicated that the ENSO modulation of the QBO requires a relatively high horizontal resolution, and that it does not show up in the climate models with parameterized but temporally constant gravity wave sources. Here, we demonstrate that the NASA GISS E2.2 models can capture the observed ENSO modulation of the QBO period with a horizontal resolution of 2° latitude by 2.5° longitude but with its gravity wave sources being parameterized interactively. This is because El Niño events lead to more vigorous gravity wave sources generating more absolute momentum fluxes over the equatorial belt, as well as less filtering of these waves into the tropical lower stratosphere through a weakening of the Walker circulation. Various components of the ENSO system such as the SSTs, the convective activities, and the Walker circulation are intimately involved in the generation and propagation of parameterized gravity waves, through which ENSO modulates the QBO period in GISS E2.2 models.

1. Introduction

The QBO dominates the interannual variability in the tropical stratosphere (Baldwin et al., 2001) while ENSO is the primary mode of interseasonal–interannual variability over the tropical Pacific Ocean (Wang et al., 2016). It is well-known that both the QBO and the ENSO have far-reaching implications for global weather and climate systems (Hamilton et al., 2015; Philander, 1990; Sarachik and Cane, 2010; Domeisen et al., 2019).

The QBO and the ENSO defy linear relationships (Angell, 1986; Xu, 1992; Hu et al., 2012) as highlighted by that fact that while the QBO and ENSO indices are negatively correlated before 1980s and positively correlated after 1980s (Garfinkel and Hartmann, 2007; Domeisen et al., 2019; Rao et al., 2020c) they are virtually uncorrelated over the longer periods from 1953 to recent times (Garfinkel and Hartmann, 2007; Geller et al., 2016b, see their Figure 5 for details) because of the apparent cancelation. However, Maruyama and Tsuneoka (1988) spotted an intriguing connection between the anomalously short easterly phase of the QBO at 50 hPa in 1987 and the El Niño event that persisted through that year. Based on the results from a mechanistic model, Geller et. al (1997) suggested that the equatorial sea surface temperatures (SST) modulate the wave momentum fluxes into the stratosphere and thus the QBO. Remarkably, an observational study conducted by Taguchi (2010) demonstrated that the downward propagation of the QBO tends to speed up during El Niño and slow down during La Niña while the amplitude of the QBO tends to be smaller during El Niño and larger during La Niña, respectively. Using radiosonde data from 10 near-equatorial stations distributed along the Equator, Yuan et al. (2014) found that the ENSO modulation of the QBO period is more robust than that of the QBO amplitude, which is likely due to the fact that the QBO periods are characterized by a high degree of zonal uniformity whereas the QBO amplitudes exhibit the zonal asymmetries of about 10% (Hamilton et al., 2004, see their Fig. 15).

The QBO influences the distribution and transport of various chemical constituents (Zawodny and McCormick, 1991; Trepte and Hitchman, 1992; Hasebe, 1994; Kawatani et al., 2014), the extratropical circulation in the winter stratosphere (Holton and Tan, 1980; Labitzke, 1982; Rao et al., 2020a, 2020b, 2021), tropical moist convection (Collimore et al., 2003; Liess and Geller, 2012), the activities of tropical cyclones (Gray et al., 1984; Ho et al., 2009), the ENSO (Gray et al., 1992; Huang et al., 2012; Hansen et al. 2016), the Hadley circulation (Hitchman and Huesmann, 2009), the tropospheric subtropical jet (Garfinkel and Hartmann, 2011a, 2011b; Kumar et al., 2022), the boreal summer monsoon (Giorgetta et al., 1999; Yoden et. al 2023), and the Madden-Julian Oscillation (Yoo and Son, 2016). Thus, it is imperative that weather and climate models have the capacity to simulate the ENSO modulation of the QBO.

Various studies have investigated how the ENSO exerts its influence over the QBO in climate models. Schirber (2015) conducted two sets of experiments to explore this issue using the general circulation model European Centre/Hamburg 6 (ECHAM6) wherein a convection-based gravity wave (GW) scheme was newly implemented. The first set of experiments was called QBOW where the initial QBO configurations consisted of a westerly jet above the 10 hPa level and an easterly jet below that level. Likewise, in the second set of experiments named as QBOE, the initial QBO conditions included an easterly and westerly jet above and below the 10 hPa level, respectively. Schirber showed that for QBOW, the ensemble mean period of the QBO from the El Niño runs is shorter than that from the La Niña runs while for QBOE, the ensemble mean periods are comparable between the El Niño and the La Niña runs. Schirber also noted that there is no systematic change in amplitude of the QBO jets between El Niño and La Niña runs. Using version 3 of the EC-Earth Consortium's climate model with a triangular spectral truncation at total wavenumber 255 (T255, horizontal resolution of ~0.54°), Christiansen et al. (2016) reported that each of ten ensemble members simulated a faster QBO descent rate during El Niño than

during La Niña, and that their ensemble mean QBO phase speeds were comparable to those derived from the reanalyses.

Employing two atmospheric general circulation models (AGCM) developed under the Model for Interdisciplinary Research on Climate (MIROC) framework, Kawatani et al. (2019) investigated the possible mechanism of the ENSO modulation of the QBO. They first compared a 100-year perpetual El Niño run with a 100-year perpetual La Niña run from the MIROC-AGCM with T106 horizontal resolution and 500-m vertical spacing in the stratosphere without any nonorographic GW parameterizations. Then they repeated the two AMIP-style perpetual El Niño and La Niña experiments but using the atmospheric part of the Model for Interdisciplinary Research on Climate, Earth System Model (MIROC-ESM) with T42 horizontal resolution and 700-m vertical spacing in the stratosphere where the effects of nonorographic GWs are parameterized and the GW sources are held constant in time. They found that the MIROC-AGCM simulates shorter QBO periods during El Niño than during La Niña because of the larger equatorial vertical wave fluxes of zonal momentum in the uppermost troposphere and consequently the much larger resolved GW forcing in the stratosphere during warm ENSO phase. However, they found almost no difference in the average QBO periods simulated by the MIROC-ESM between El Niño and La Niña because the QBO was generated by the parameterized nonorographic GW forcing in the model where the GW sources were held constant in time, thus did not respond to the SST changes associated with the ENSO cycle (See their Figs. 16 and 18 for more details).

Using more than a dozen of models from five modeling centers with their horizontal resolutions ranging from T42 (~2.79°) to T1279 (~0.14°), Serva et al. (2020) found that a relatively high horizontal resolution above T159 (~0.75°) was desirable to simulate the observed modulation of the QBO descent rate under strong ENSO events, while the amplitude response is generally weak at any horizontal resolution. They also pointed out that over-dependence on parameterizing the effects of GWs with

temporally invariant sources is detrimental to the realistic simulation of the coupling between the ocean and the tropical stratosphere in current climate models.

As far as the ENSO modulation of the QBO period is concerned, both Kawatani et al. (2019) and Serva et al. (2020) emphasized the importance of a relatively high horizontal resolution and the inadequacy of non-interactive GW sources. However, the exploratory work of Schirber (2015) shows that the ENSO modulation of the QBO period can, to some extent, be simulated in the GCM ECHAM6 with T63 and an associated Gaussian grid of ~1.9° horizontal resolution because rather than being held constant in time, the properties of non-interactive GW sources in the tropics are determined by the simulated convection which is modulated by ENSO phases.

Rind et al. (1988) pioneered the use of meteorologically interactive GW sources in the Goddard Institute for Space Studies (GISS) climate models. These sources included flow over topography, convection, shear, and, in Rind et al. (2007), deformation. By increasing the vertical resolution and revising the formulations, various versions of the GISS models subsequently simulate a spontaneous QBO (Rind et al., 2014, 2020; DallaSanta et al., 2021). The GISS E2.2 models are comprehensive climate models optimized for the middle atmosphere (Rind et al., 2020; Orbe et al., 2020). Their outputs have been submitted to the archive of the Coupled Model Intercomparison Project Phase 6 (CMIP6). Bushell et al. (2020) pointed out that most of current climate models are highly dependent on parameterized nonorographic GW forcing to simulate a QBO. Unsurprisingly, DallaSanta et al. (2021) found that the parameterized convective GWs play a dominant role in generating the spontaneous QBO in the GISS E2.2 models.

High-resolution AGCMs can realistically simulate atmospheric structure without resorting to parameterized GWs (e.g., Watanabe et al., 2008), but the associated computational cost is too high for the Earth system modeling at the present time. Thus, most climate models still require GW

parameterization schemes. What is more, Fig. 4(c) in Serva et al. (2020) shows that two different GW parameterization schemes employed by the same T255 model make a drastic difference in the ENSO modulation of the QBO period. Specifically, one scheme makes a difference of about 10 months in the ensemble mean QBO period between El Niño and La Niña episodes while the other hardly makes an appreciable difference. In other words, improperly parameterized GW forcing could destructively interfere with the ENSO modulation of the QBO period in high-resolution climate models. Therefore, it is imperative that GWs forcing be parameterized properly in climate models with a variety of horizontal resolutions.

In this paper, we will evaluate the ENSO modulation of the QBO simulated by the GISS E2.2 models against the observed and explore how the ENSO modulates the QBO period in those models. Section 2 describes the observations and GISS E2.2 models used in this study and outlines our methods of analyses. Section 3 revisits the ENSO modulation of the QBO from the observational point of view. Section 4 evaluates the ENSO modulation of QBO period in the historical runs simulated by four versions of the GISS E2.2 models. Section 5 explores the physical mechanisms underlying the simulated modulation. Conclusions and discussion are presented in section 6.

2. Observations, model simulations, and methods

2.1 Observations

To study the observed QBO, we use the monthly mean zonal winds provided by Free University of Berlin (FUB). The FUB data were produced by combining the radiosonde observations at the following three equatorial stations: Canton Island near 172°W, 3°S (closed in 1967), Gan/Maledive Islands near 73°E, 1°S (closed in 1975), and Singapore near 104°E, 1°N (Naujokat, 1986). We use 63 years (i.e., 756

months) of the FUB data ranging from 1953 to 2015 at the following seven pressure levels: 70, 50, 40, 30, 20, 15, and 10 hPa.

The observed ENSO index is derived from the National Oceanic and Atmospheric Administration (NOAA) Extended Reconstructed SST (ERSST) V5 datasets (Huang et al., 2017) provided by National Centers for Environmental Information (NCEI). ERSST produced on a $2° \times 2°$ grid is derived from the International Comprehensive Ocean-Atmosphere Data Set (ICOADS). The latest version of ERSST, version 5, uses new datasets from ICOADS Release 3.0 SST, combining information from Argo floats above 5 m and Hadley Centre Ice-SST version 2 ice concentrations.

The monthly Outgoing Longwave Radiation (OLR) on a $2.5° \times 2.5°$ grid from NCEI is used as a proxy for tropical convection since cloud top temperatures are negatively correlated with cloud height in the tropics (Salby, 2012). The ERA5 (Hersbach et al., 2020) monthly mean zonal winds were employed to depict the observed Walker circulation against which we evaluate those simulated by GISS E2.2 models. The employed OLR and zonal winds range from 1979 to 2015.

2.2 Description of the models and simulations

GISS E2.2 is a climate model specially optimized for the middle atmosphere (Rind et al., 2020; Orbe et al., 2020) and its output was submitted to the Coupled Model Intercomparison Project Phase 6 (CMIP6) archive. The horizontal resolution of all GISS E2.2 models is 2° (latitude) × 2.5° (longitude) for the atmosphere and the model extends from the surface to 0.002 hPa (~89 km) with 102 vertical layers (for more details, see Table 1 in Rind et al., 2020). Note that an adequate vertical resolution is necessary for climate models to internally generate a spontaneous QBO (Scaife et al., 2000; Richter et al. 2014; Rind et al, 2014, 2020; Geller et al. 2016a; Butchart et al. 2018).

According to composition interactivity, the atmospheric component of the GISS E2.2 models was configured in two ways for CMIP6. The first configuration is denoted as NonINTeractive ("NINT")

where the fields of radiatively active components such as ozone and multiple aerosol species are specified from previously calculated offline fields (Kelley et al. 2020; Miller et al., 2021), which will be discussed further below. The second configuration includes interactive gas-phase chemistry and a mass-based (One-Moment Aerosol, OMA) aerosol module, where aerosols and ozone are driven by emissions and calculated prognostically (Bauer et al., 2020; Nazarenko et al., 2022). The abovementioned NINT and OMA configurations correspond to physics-version=1 ("p1") and physics-version=3 ("p3"), respectively, in the CMIP6 archive.

The basic dynamics and tropospheric physics structure of the GISS E2.2 models were based on the GISS E2.1 model (Kelley et al., 2020). One version of the cloud parameterization schemes used in E2.2, termed as "standard physics" (SP), has not been fully upgraded to the state-of-the-art module customized for E2.1 which has only 40 vertical layers up to 0.1 hPa (Rind et al., 2020). Accordingly, E2.2–SP has a younger sibling, E2.2–AP, whose cloud parameterization schemes, termed as "Altered Physics" (AP), are more aligned with those in E2.1 and whose outputs were thus favored for the submission to the CMIP6 archive. "Altered Physics" in E2.2–AP brings about a somewhat different response to SST as compared with the "standard physics" in E2.2–SP.

The QBO in the GISS models are mainly driven by GWs (DallaSanta et al., 2021). The phase velocities and momentum fluxes of GW sources are coupled to convective cloud-top-pressure altitudes, convective mass fluxes, background wind fields, etc. (Rind et al., 1988, 2014, 2020). Specifically speaking, intrinsic phase velocities $\pm 10\, ms^{-1}$ and $\pm 20\, ms^{-1}$ of GWs generated by convection are Doppler-shifted by local background winds for shallow convection and for convection penetrating above the altitudes of the 400-hPa pressure level, respectively. Convective gravity wave momentum flux magnitude is determined by the density and Brunt-Vaisala frequency at the top of convective region and the vertically integrated mass flux over the convective region. The mass flux in the model is strongly

related to the depth of penetration, and thus this parameterization is somewhat similar to that of the other models that use convective sources (see Eq. 7 in Rind et al., 1988 and the further discussion in Rind et al., 2014).

Using the same GW parameterization scheme, both E2.2–SP and E2.2–AP are included in this study to gain insight into the mechanisms through which ENSO modulates the QBO period despite the fact that the outputs of E2.2–SP were not submitted to the CMIP6 archive. Note that outputs from E2.2–SP models, following the CMIP6 protocol and naming, are available from the NASA Center for Climate Simulation (NCCS) portal (under the title E2.2.1).

In this study we look into two atmosphere-only (AMIP) ensemble simulations where the evolution of SST and sea ice fraction (SIF) is specified and two coupled ensembles where the respective model atmosphere interacts with the ocean component termed as the GISS Ocean v1 (GO1) which extends from the surface to the ocean floor with 40 vertical layers and has a horizontal resolution of 1° latitude by 1.25° longitude (Schmidt, et al., 2014; Kelley et al., 2020). Table 1 lists the four model configurations and their respective ensemble simulations investigated in this study.

The first two ensembles in Table 1 were generated by AMIP–OMA–SP and AMIP–OMA–AP models where the SST and SIF from the HadISST1 dataset (Rayner et al., 2003) were prescribed for the simulations between 1870 and 2014 while their climatological annual cycles over the 1876–1885 period were imposed for the earlier simulations between 1850 and 1869. Both AMIP–OMA–SP and AMIP–OMA–AP prognostically calculate the concentrations of ozone, methane, chlorofluorocarbons, aerosols, etc. The main differences between AMIP–OMA–SP and AMIP–OMA–AP reside in the package of cloud parameterization schemes, which leads to their different responses to SST and thus may have important implications for simulating the ENSO modulation of the QBO period. We discarded the simulations ranging from 1850 to 1869 in this study because they are irrelevant to the ENSO modulation of the QBO

in the absence of interannual variations in the prescribed SST over that period. Note that the two extended historical AMIP simulations from 1870 to 2014 listed in Table 1 were not submitted to the CMIP6 archive. However, AMIP–OMA–AP did generate a 5-member ensemble over the 1979–2014 period that was submitted to the CMIP6 archive and tagged as E2-2-G.amip.r[1-5]i1p3f1. It is worth noting that the climatological characteristics over the 1979–2014 period derived from the AMIP–OMA–AP ensemble listed in Table 1 are comparable to those derived from E2-2-G.amip.r[1-5]i1p3f1 albeit the climate trajectories of the individual ensemble members over the 1979–2014 period are expected to differ between those two ensembles starting from January 1850 and January 1979, respectively, due to the chaotic nature of climate systems.

The other two ensembles in Table 1 were generated by the Coupled–NINT–SP and Coupled–NINT–AP where the respective atmospheric components are coupled with GO1. Both the Coupled–NINT–SP and Coupled–NINT–AP simulations were performed with the prescribed atmospheric composition generated from the AMIP-style OMA simulations using the historical forcings over the 1850–2014 period. As mentioned earlier with regard to the AMIP–OMA–SP and AMIP–OMA–AP runs, the difference in cloud physics between the Coupled–NINT–SP and Coupled–NINT–AP models is exploited to gain a deeper insight into the mechanisms through which the ENSO modulates the QBO periods. Both Coupled–NINT–SP and Coupled–NINT–AP ensemble runs started from January 1850 and ended in December 2014.

Since there are no interannual variations in the prescribed SST over the 1850–1869 period for both the AMIP–OMA–SP and AMIP–OMA–AP runs, our analyses focus on the 1870–2014 period for those two ensembles. For the sake of conciseness and consistency, we also discarded the outputs from two coupled runs over the 1850–1869 period. In short, we only use the data over the 1870–2014 period from the ensemble simulations listed in Table 1.

2.3 Methods

2.3.1 Data processing

We first fill the missing FUB zonal winds at the 10 hPa level for the first 3 years by linear extrapolation in log-pressure height. Then, we remove the climatological mean zonal winds from the observed to obtain the monthly anomalies of zonal winds. These anomalous monthly zonal winds will be used for our observational study in this paper.

To obtain the ENSO index from the ERSSTv5 data ranging from 1953 to 2015, we use the same method to calculate the Oceanic Niño Index (ONI) as the Climate Prediction Center (CPC) of NOAA. Namely, the ONI is defined as a 3-month running mean of ERSSTv5 SST anomalies in the Niño 3.4 region (5°S – 5°N, 120° – 170°W) based on centered 30-year base periods updated every 5 years (https://origin.cpc.ncep.noaa.gov/products/analysis_monitoring/ensostuff/ONI_v5.php). This method ensures a proper identification of El Niño and La Niña by taking the secular changes in SSTs into account. The SST anomalies are defined as the deviations of the SST from its climatological annual cycle over a selected base period. Specifically, the SST anomalies during 1951–1955 are based on the 1936–1965 base period; the SST anomalies during 1956–1960 are based on the 1941-1970 base period; and so on. Thus, as the CPC of NOAA we used the ERSSTv5 SST from January 1936 to January 2016 period to obtain the ONI from January 1953 to December 2015.

Following the CPC of NOAA, we refer to El Niño or La Niña episodes as the periods when the ONIs are greater than +0.5°C or less than –0.5°C for at least five consecutive months, respectively. Since the temperature measurement is only accurate to the tenths place, all our calculated ONIs are rounded to the nearest tenth. Based on the rounded ONIs, our identified El Niño and La Niña episodes are almost identical to those listed at the abovementioned website of NOAA CPC. Accordingly, we identified 21 El Niño and 15 La Niña events between 1953 and 2015.

Similarly, when we explore how GISS E2.2 models simulate the ENSO modulation of the QBO we define the ONI as a 3-month running mean of prescribed SST anomalies from the AMIP–OMA–SP and AMIP–OMA–AP runs, or simulated SST anomalies from the Coupled–NINT–SP and Coupled–NINT–AP runs in the Niño 3.4 region (5°S – 5°N, 120° – 170°W) based on centered 30-year base periods updated every 5 years. Here, the SST anomalies are also defined as the deviations of the SST from its climatological annual cycle over a selected base period. Specifically, the SST anomalies during 1886–1890 are based on the 1871–1900 base period; the SST anomalies during 1891–1895 are based on the 1876-1905 base period; the SST anomalies during 1991–1995 are based on the 1976-2005 base period; the SST anomalies during 1996–2000 are based on the 1981–2010 base period. In addition, the SST anomalies during the earliest 1870–1885 and latest 2011–2014 spans are ad hoc based on the 1870–1899 and 1985–2014 base periods, respectively. Thus, we used the specified or simulated SSTs over the 1870–2014 period to obtain the ONI from February 1870 to November 2014.

For the sake of consistency, we also apply this same filtering procedure to all other fields simulated by GISS E2.2 models such as OLR, zonal winds, resolved wave forcing, parameterized GW forcing, absolute convective momentum flux, etc. Thus, the simulated zonal winds and other quantities were subjected to a 3-month moving averaging. In addition, the secular trends of zonal winds and those quantities were also removed due to the adoption of the consecutive 5-year base periods. To further simplify our analyses, all processed model outputs used in this study range from 1871 to 2013. In other words, we also discarded the processed model outputs over the period between February 1870 to December 1870 and that between January 2014 to November 2014.

Employing the above-mentioned criterion that was used to identify the observed ENSO events between 1953 and 2015, we identified 34 El Niño and 30 La Niña events over the period from 1871 to 2013 from the specified HadISST1 dataset. We further found that the five members of the Coupled–

NINT–SP ensemble simulations generated 31, 31, 29, 35, and 36 El Niño events and produced 34, 34, 35, 37, and 35 La Niña events, respectively, over the period from 1871 to 2013. In parallel, we identified 37, 42, 40, 37, and 38 El Niño events and 38, 43, 37, 40, and 39 La Niña events from the SSTs simulated by the five members of the Coupled–NINT–AP ensemble, respectively, over the same period.

2.3.2 Statistical analysis

Following Wallace et al. (1993), we decompose the zonal winds from both the observed and the simulated between 10 and 70 hPa pressure levels into two leading pairs of empirical orthogonal functions (EOFs) and principal components (PCs) because they typically account for more than 90% of the vertical structure variance (Wallace et al., 1993; DallaSanta et al., 2021). For the sake of robustness, we excluded the FUB data after 2015 because the first two EOFs explain no more than 60% of total variance during the 2016 and 2019/20 QBO disruptions (Anstey et al., 2021). As a result, the QBO variability can be, to a very good approximation, compactly depicted by the trajectory of $\left(PC_1(t), PC_2(t)\right)$ in a linear space spanned by the first two orthonormal EOFs.

As in previous studies (Wallace et al., 1993; Taguchi, 2010, Christiansen et al. 2016; Serva et al. 2020; DallaSanta et al., 2021), the instantaneous amplitude (am) and phase (ψ) of the QBO are defined as

$$am = \sqrt{PC_1^2 + PC_2^2} \tag{1}$$

$$\psi = atan2(PC_2, PC_1) \tag{2}$$

Differentiating (2) with respect to time yields the instantaneous phase speed of the QBO:

$$\psi' = (PC_1 \cdot PC_2' - PC_1' \cdot PC_2)/(PC_1^2 + PC_2^2) \tag{3}$$

Using Eqs. (1) – (3) and the monthly processed FUB data from 1953 to 2008, Taguchi (2010) obtained 672 months of am and ψ' and partitioned each time series of $\{am\}$ and $\{\psi'\}$ into 16 categories. The 16 categories correspond to the 16 combinations of four QBO phase quadrants at the 50-hPa level

and four seasons. Using a bootstrap (Chernick, 2007) method, Taguchi (2010) seminally illuminated the annual synchronization of the QBO. Taguchi (2010) further used the bootstrap method to show that the QBO signals during El Niño episodes exhibit weaker amplitude in six out of 16 categories and faster phase propagation in eight out of 16 categories at a 90% or 95% confidence level (refer to Figure 6 in Taguchi, 2010).

It is worth pointing out that while Taguchi's conclusion is physically meaningful, his statistical analysis is not robust concerning the ENSO influence on the QBO. For instance, there are 18 sample points in the (MAM, E) category where MAM stands for the months of boreal spring, i.e., March, April, and May while E indicates the QBO winds at the 50-hPa level are easterly. As Taguchi (2010) mentioned that the actual sample size should be six rather than 18 due to the data clustering. Among those 18 months of data, there are six for El Niño conditions and one for La Niña condition. Also pointed out by Taguchi (2010), actually sample sizes are two and one for El Niño and La Niña conditions, respectively, in the (MAM, E) category. It is hard to imagine we can infer any meaningful result from one La Niña sample point and two El Niño sample points out of the sample with its size being nine because Chernick (2007) points out that samples of size less than 10 are usually too small to rely on sample estimates, even in "nice" parametric cases, and that we should expect that such sample sizes are also too small for bootstrap estimates to be of much use (see his page 174). With regard to the above-mentioned (MAM, E) category, the following conclusion is evidently not robust: the QBO amplitude during El Niño episodes is weaker than that during La Niña episodes at a 95% confidence level (refer to Figure 6(b) in Taguchi, 2010) because one extreme La Niña and/or a couple of extreme El Niño sample points can influence the outcome of the statistical test.

Since we have observed 21 El Niño and 15 La Niña events between 1953 and 2015, the sample sizes of El Niño and La Niña appear large enough for us to conduct a classical parametric test. Namely, we

have two sample spaces: one consists of 21 independent El Niño events and the other contains 15 independent La Niña events. For each ENSO event, we define the amplitude (A) and phase speed (Ψ') of the QBO as the monthly am in Eq. (1) and the monthly ψ' in Eq. (3) that are averaged over the number of months of that event. Thus, two random variables A and Ψ', i.e., the mean amplitude and mean phase speed of the QBO during an ENSO episode, are defined both on the El Niño sample space and on the La Niña sample space. We employ Welch's *t*-test (Moser and Stevens, 1992) to examine whether there is a significant difference in A or Ψ' between the El Niño and La Niña population means.

To examine whether the sample mean QBO amplitude is significantly different between El Niño and La Niña, we first construct the statistic:

$$t = \frac{\bar{A}_1 - \bar{A}_2}{s_{\bar{A}_1 - \bar{A}_2}} \tag{4}$$

where $\bar{A}_1$ and $\bar{A}_2$ are the values of As that are averaged over the number of the El Niño and La Niña events, respectively.

$$s_{\bar{A}_1 - \bar{A}_2} = \sqrt{\frac{s_{A_1}^2}{N_1} + \frac{s_{A_2}^2}{N_2}} \tag{5}$$

where s_{A_1} and s_{A_2} are the corrected sample standard deviation of A for El Niño and La Niña, respectively while N_1 and N_2 are the sample sizes of El Niño and La Niña events. According to Moser and Stevens (1992), the degrees of freedom for the *t*-distribution is

$$\nu = \frac{\left(s_{A_1}^2/N_1 + s_{A_2}^2/N_2\right)^2}{\left(\frac{s_{A_1}^2}{N_1}\right)^2/(N_1-1) + \left(\frac{s_{A_2}^2}{N_2}\right)^2/(N_2-1)} \tag{6}$$

2.3.3 Analysis of the QBO forcings

The QBO owes its existence to wave-mean flow interaction (Lindzen and Holton, 1968; Holton and Lindzen,1972; Plumb, 1977). The evolution of zonal mean zonal winds is governed by the transformed-Eulerian-mean (TEM) momentum equation formulated in pressure coordinates on a sphere (Andrews et al., 1983):

$$\frac{\partial \overline{u}}{\partial t} = \overline{G} + \frac{1}{\rho_0 a \cos\varphi}\vec{\nabla}\cdot\vec{F} - \left\{\frac{\overline{v}^*}{a\cos\varphi}\left[\frac{\partial}{\partial\varphi}(\overline{u}\cos\varphi) - f\right] + \overline{\omega}^*\frac{\partial \overline{u}}{\partial p}\right\} + \overline{X}, \quad (7)$$

where the Eliassen-Palm flux $\vec{F}$ is defined as

$$\vec{F} = \left\{F^{(\varphi)}, F^{(p)}\right\} = a\cos\varphi\left\{-\overline{u'v'} + \psi\overline{u}_p, -\overline{u'\omega'} - \varepsilon[(a\cos\varphi)^{-1}(\overline{u}\cos\varphi)_\varphi - f]\right\}, \quad (8)$$

and its divergence as

$$\vec{\nabla}\cdot\vec{F} = \frac{1}{a\cos\varphi}\frac{\partial}{\partial\varphi}\left(F^{(\varphi)}\cos\varphi\right) + \frac{\partial F^{(p)}}{\partial p}. \quad (9)$$

In Eq. (7), t denotes time, p pressure, φ latitude, (u, v, ω) "velocity" in (longitude, latitude, pressure) coordinates, a the mean radius of Earth, ρ_0 pressure-dependent basic density, and f the Coriolis parameter. In Eq. (8), ε is defined as

$$\varepsilon = \overline{v'\theta'}/\overline{\theta}_p = -\overline{v'T'}/(\frac{\kappa\overline{T}}{p} - \frac{\partial\overline{T}}{\partial p}), \quad (10)$$

where θ denotes potential temperature, T temperature, and κ the ratio of the gas constant to the specific heat at constant pressure. Note that in Eqs. (7) – (10) primes denote departures from the zonal means which are represented by overbars, and residual meridional and vertical velocities, i.e., $\overline{v}^*$ and $\overline{\omega}^*$, are defined as $(\overline{v} - \frac{\partial\psi}{\partial p})$ and $(\overline{\omega} + \frac{1}{a\cos\varphi}\frac{\partial(\varepsilon\cos\varphi)}{\partial\varphi})$, respectively.

On the right hand side (RHS) of Eq. (7), the first term, $\overline{G}$, is the forcing from the GWs parameterized in E2.2 models; the second term, $\frac{1}{\rho_0 a\cos\varphi}\vec{\nabla}\cdot\vec{F}$, is the forcing driven by the waves resolved by GISS E2.2 models; the third term, $-\left\{\frac{\overline{v}^*}{a\cos\varphi}\left[\frac{\partial}{\partial\varphi}(\overline{u}\cos\varphi) - f\right] + \overline{\omega}^*\frac{\partial\overline{u}}{\partial p}\right\}$, is associated with the TEM

361 advection; and last term, $\overline{X}$, is the zonal component of friction or other nonconservative mechanical
362 forcing (Andrews et al., 1987). Since $\overline{X}$ is small as far as the QBO is concerned , we will focus on
363 analyzing the first three terms of Eq. (7) and ignore the last term of that equation in this study.
364
365 **3. Revisiting the ENSO modulation of the QBO from observations**
366 In the era of big data, bootstrap methods are a powerful tool that is used to analyze uncertainties for
367 any machine learning model. However, the bootstrap methods cannot get something for nothing. It is
368 not reliable if sample size is too small. In this section, we will use the classical parametric method
369 outlined in subsection 2.3.2 to revisit the ENSO modulation of the QBO using the FUB data described
370 in subsection 2.1.
371 The solid and dashed black lines in Fig. 1 depicts the two leading EOFs derived from the monthly
372 anomalies of the FUB zonal winds between 1953 and 2015. The vertical structures of those two EOFs
373 are very similar to those depicted in Fig. 2a of Taguchi (2010) who used the FUB zonal winds from 1953
374 to 2008. Our calculated two leading EOFs account for 92.6% of the vertical structure variance (57.1%
375 by EOF1 and 35.5% by EOF2) which is slightly smaller than the value of 96.1% shown in Taguchi
376 (2010). Note that this discrepancy is not mainly due to the difference in the adopted time spans. When
377 we use the monthly anomalies of the FUB zonal winds between 1953 and 2008, the resultant two leading
378 EOFs account for 92.9% of the vertical structure variance (57.0% by EOF1 and 35.9% by EOF2). Coy
379 et al. (2020) pointed out that the descent of the QBO winds varies at intraseasonal, seasonal, and
380 interannual time scales (see their Figure 1 for more details). Thus, it is natural that two leading EOFs
381 explain more variance of the FUB zonal winds when those winds have been deseasonalized and
382 subjected to a 5-month running averaging.

As mentioned before, there are 21 El Niño and 15 La Niña episodes between 1953 and 2015, i.e., $N_1 = 21$ and $N_2 = 15$. Our calculations yield $\bar{A}_1 = 39.5\, ms^{-1}$, $\bar{A}_2 = 42.4\, ms^{-1}$, $\nu = 33$, and $t = -1.50$. Apparently, $\bar{A}_1 < \bar{A}_2$, which suggests that the QBO amplitude is smaller during El Niño than during La Niña. Performing a two-tailed test, however, we find that the QBO amplitudes during El Niño episodes are not statistically different from those during La Niña episodes at the 10% significance level. This is consistent with the finding of the observational study by Yuan et al. (2014), namely, the ENSO modulation of the QBO amplitude is less robust than that of the QBO period. This is also consistent with the findings of the modeling studies conducted by Schirber (2015) and Serva (2020).

Note that when we use the FUB zonal winds and the ERSSTv5 data over the 1953–2008 period as Taguchi (2010), our calculations yield $N_1 = 19$, $N_2 = 13$, $\bar{A}_1 = 39.1\, ms^{-1}$, $\bar{A}_2 = 43.1\, ms^{-1}$, $\nu = 29$, and $t = -1.98$. A two-tailed test shows that the difference of the QBO amplitude between El Niño and La Niña is not statistically significant at the 5% significance level.

Apparently, no matter whether we use the FUB data over the 1953–2008 period or over the 1953–2015 period, the influence of the ENSO on the QBO amplitude is not statistically significant at the 5% significance level. Thus, we will not further explore whether GISS E2.2 models can simulate the ENSO modulation of the QBO amplitude in this study.

To examine whether the sample mean QBO phase speed is significantly different between El Niño and La Niña, we similarly use Eqs. (4) – (6) except that $\bar{A}_1$ and $\bar{A}_2$ are replaced by $\overline{\Psi_1'}$ and $\overline{\Psi_2'}$, respectively. Based on the data from 1953 to 2015, we obtained $N_1 = 21$ and $N_2 = 15$, $\overline{\Psi_1'} = 0.246$ radians/month, $\overline{\Psi_2'} = 0.183$ radians/month, $\nu = 28$, and $t = 2.36$. Evidently, $\overline{\Psi_1'} > \overline{\Psi_2'}$, indicating that the phase speed of the QBO is greater during El Niño than during La Niña. Performing a two-tailed test, we ascertain that the phase speed of QBO during El Niño episodes are statistically different from those during La Niña episodes at the 5% significance level. Put in another way, the mean QBO period of 25.6

406 months (i.e., $2\pi/0.246$) during El Niño is statistically shorter than that of 34.3 months (i.e., $2\pi/0.183$)
407 during La Niña over the 1953–2015 period. Furthermore, when we use the FUB zonal winds and the
408 ERSSTv5 data over the 1953–2008 period as Taguchi (2010), our calculations yield $N_1 = 19$ and $N_2 =$
409 13, $\overline{\Psi_1'} = 0.253$ radians/month, $\overline{\Psi_2'} = 0.180$ radians/month, $\nu = 25$, and $t = 2.87$. Apparently, we
410 reach a similar conclusion that the mean QBO period of 24.8 months (i.e., $2\pi/0.253$) during El Niño is
411 statistically shorter than that of 34.9 months (i.e., $2\pi/0.180$) during La Niña at the 5% significance level.
412 Thus, no matter whether we use the FUB data over the 1953–2008 period or over the 1953–2015
413 period, the influence of the ENSO on the QBO phase speed is statistically significant at the 5%
414 significance level. In other words, our observational study robustly buttresses the following conclusion
415 of Taguchi (2010): the QBO descent is faster during El Niño than during La Niña. Henceforth, we will
416 focus only on the ENSO modulation of the QBO period in this study.
417 To facilitate comparison with other studies (e.g., Taguchi, 2010; Christiansen et al., 2016; Serva et
418 al. 2020), we also calculate the mean phase speed of the QBO by averaging monthly ψ' in Eq. (3) over
419 all the 210 months of the El Niño episodes and over all the 201 months of the La Niña episodes between
420 1953 and 2015. Subsequently, we obtain the mean QBO period of 25.6 months during El Niño and of
421 32.2 months during La Niña for the 1953–2015 period. Similarly, we obtain the mean phase speed of the
422 QBO by averaging monthly ψ' in Eq. (3) over all the 186 months of the El Niño episodes and over all
423 the 174 months of the La Niña episodes for the 1953–2008 period. The resultant values are 24.9 and 32.2
424 months, respectively, which are very close to 25 and 32 months inferred by Taguchi (2010). No matter
425 whether the selected FUB data span from 1953 to 2008 or range from 1953 to 2015, we robustly conclude
426 that the QBO descent rate is faster during El Niño than during La Niña.
427 Note that it is difficult to rigorously determine the degrees of freedom for a *t*-test when we choose the
428 monthly data as sample points which share some common characteristics, i.e., are not independent of

each other during an ENSO event (for more details, refer to Taguchi, 2010). In the remainder of this paper, when we need to conduct a Welch's *t*-test we choose the QBO period averaged over each ENSO episode as a sample point. Otherwise, the mean values during El Niño or La Niña are referred to the quantities averaged over all the months of El Niño or La Niña category in alignment with previous works conducted by Taguchi (2010), Christiansen et al. (2016), and Serva et al. (2020).

The QBO is mainly driven by tropical waves (Lindzen and Holton, 1968; Holton and Lindzen, 1972; Plumb 1977) of which tropical convection is an important source (Holton, 1972; Salby and Garcia, 1987; Bergman and Salby, 1994; Tsuda et al., 2009; Alexander et al., 2017). To investigate how tropical convection is influenced by the ENSO, we first produce the monthly anomalies of OLR from NOAA NCEI over the 1979–2015 period. Then we obtain the mean OLR anomalies for La Niña and El Niño conditions by averaging the monthly OLR anomalies over all the months that fall into La Niña and El Niño categories, respectively. Fig. 2a show that mean OLR anomalies exhibit a broad and positive pattern that spans the central and eastern equatorial Pacific and a negative pattern in the maritime continent for the La Niña conditions. In contrast, Fig. 2b show that they exhibit a broad and negative pattern that spans the central and eastern equatorial Pacific and a positive pattern in the maritime continent for the El Niño conditions. The large differences in the mean OLR anomalies in Fig. 2c between El Niño and La Niña conditions are closely related with the contrast in the SST anomalies patterns shown in Fig. 3. Namely, the distinctive patterns of positive and negative SST anomalies extend over the central and eastern Pacific during the El Niño and La Niña episodes, respectively, which not only gives rise to the corresponding positive and negative rainfall anomalies (Philander, 1990) and the concomitant OLR anomalies shown in Fig. 2, but also leads to various teleconnections outside the tropics (Domeisen et al., 2019).

In the next section, we will evaluate how the ENSO modulates the QBO periods in the E2.2 models and whether those models can realistically capture the contrast in the OLR (and convection) patterns that generally underlies the difference in wave driving of the QBO between warm and cold ENSO conditions.

4. ENSO modulation of the QBO period in GISS E2.2 models

Now we investigate the ENSO modulation of the QBO period in the ensemble simulations listed in Table 1.

We first calculate the monthly mean anomalies of zonal winds using the method outlined in subsection 2.3.1. Then we average those monthly mean anomalous zonal winds over the latitudinal belt from 5° S to 5° N to obtain the monthly QBO winds over the 1871 to 2013 period at the following seven pressure levels: 70, 50, 40, 30, 20, 15, and 10 hPa.

As in section 3, we decompose the QBO winds from 10 to 70 hPa over the 1871–2013 period into two leading pairs of empirical orthogonal functions (EOFs) and principal components (PCs). For each of the 19 ensemble simulations listed in Table 1, the first two leading EOFs account for at least 92.9% of the vertical structure variance which is comparable to the value derived from the observations discussed in section 3. Since coupled models encounter more difficulties in simulating the ENSO modulations of the QBO (Serva et al. 2020, see their Fig.4 for more details), we first look into the ensemble simulations from the Coupled–NINT–AP model, which incorporates the most up-to-date cloud parameterization schemes. The red and blue lines in Fig. 1 depicts the first two leading EOFs from each of all five Coupled–NINT–AP runs. For each of those five runs, the first two leading EOFs account for at least 93.8% of the vertical structure variance. The vertical structures of those two EOFs from each Coupled–NINT–AP run are broadly similar to the solid and dashed black lines derived from observations in Fig. 1. The respective vertical structures of the first two leading EOFs are almost identical among all

five Coupled–NINT–AP ensemble runs, which is expected because all runs share the same model and differ from each other only in their initial conditions. It is worth noting that the vertical structures of the first two leading EOFs simulated by Coupled–NINT–AP are somewhat different from those observed below the 20 hPa level because none of CMIP models could simulate a QBO in the lower stratosphere that is as strong as the observed (Richter et al., 2020). In addition, we find that the vertical structures of the first two leading EOFs from other three ensemble simulations listed in Table 1 (figures not shown) are comparable to those from the Coupled–NINT–AP runs. Thus, the simulated QBO variabilities in each ensemble can be, to a very good approximation, compactly depicted by the trajectory of $\left(PC_1(t), PC_2(t)\right)$ in a linear space spanned by the first two orthonormal EOFs.

For the ensemble simulations listed in Table 1, we define an El Niño or La Niña event according to the criterion described in subsection 2.3.1. Similarly, Eq. (3) is used to calculate the instantaneous (i.e., monthly) phase speed of the simulated QBO. For each El Niño or La Niña event, the mean phase speed of the simulated QBO from any individual run listed in Table 1 is obtained by averaging the instantaneous phase speeds of the simulated QBO over the number of months of that event. Accordingly, we have one sample space consisting of independent El Niño events and the other consisting of independent La Niña events. In addition, we employ a two-tailed Welch's *t*-test outlined in subsection 2.3.2 to examine whether there is a significant difference in the phase speed of the simulated QBO between the El Niño and La Niña population means.

Table 2 describes how the ENSO influence the QBO period in each member of all ensembles, where E[1-4] represent AMIP–OMA–SP, AMIP–OMA–AP, Coupled–NINT–SP, and Coupled–NINT–AP ensembles, respectively while r1, r2,… indicate its respective member of each ensemble. As we mentioned in subsection 2.3.1, for the member r1 of E1, i.e., the first run of the AMIP–OMA–SP ensemble, there are 34 El Niño and 30 La Niña events between 1871 and 2013, i.e., $N_1 = 34$ and $N_2 =$

30 in Eqs. (5) and (6). Then we obtained the phase speed of the QBO for each episode of those 34 El Niño and 30 La Niña events, from which we derived the mean phase speed of the QBO averaged over the 34 El Niño and 30 La Niña events, respectively. Accordingly, our mean phase speeds of the QBO simulated by r1 of E1 averaged over the El Niño and La Niña events are obtained as 0.202 radians/month and 0.185 radians/month, respectively, and the standard deviations about those mean phase speeds as 0.0345 radians/month and 0.0275 radians/month, respectively. Substituting those numbers into Eqs. $(4)-(6)$ yields $\nu = 61$, and $t = 2.25$. Therefore, the phase speed of the QBO simulated by r1 of E1 is statistically significantly greater during El Niño than during La Niña at the 5% significance level. Accordingly, we register the mean QBO period of 31.1 months (i.e., $2\pi/0.202$) during the El Niño episodes and 34.0 months (i.e., $2\pi/0.185$) during the La Niña episodes as the entries for r1 of E1 in Table 2. Since the phase speeds of the QBO simulated by r1 of E1 are statistically significantly different between the El Niño and La Niña categories at the 5% significance level, we can regard the QBO periods as being statistically significantly different between El Niño and La Niña episodes and register their difference, -2.9 months, in Table 2 with a pair of parentheses indicating this significance. Similarly, we calculated the QBO periods during ENSO extremes and their difference simulated by every member of all ensembles and registered them in Table 2 where the numbers in the parentheses indicate that the phase speed of the simulated QBO is statistically significantly greater during El Niño than during La Niña at the 5% significance level.

Table 2 shows that 18 of 19 runs from the four GISS E2.2 models listed in Table 1 can simulate the ENSO modulation of the QBO period discussed in section 3. For each Coupled–NINT–AP ensemble run, the phase speed of the simulated QBO is statistically significantly greater during El Niño than during La Niña at the 5% significance level. For the AMIP–OMA–SP and AMIP–OMA–AP ensembles, most members also generate a spontaneous QBO whose phase speed is statistically significantly greater during

El Niño than during La Niña at the 5% significance level. Intriguingly, in none of the Coupled–NINT–SP ensemble runs is the phase speed of the simulated QBO statistically significantly different between El Niño and La Niña episodes at the 5% significance level albeit the contrast in the QBO periods between the two categories simulated by r1 of E3 (i.e., Coupled–NINT–SP) is equal to -6.2 months and greater than that simulated by most members of Coupled–NINT–AP. We will look further into this issue in section 6.

5. Mechanisms of the ENSO modulation of the QBO period in GISS E2.2 models

5.1 ENSO modulation of the QBO forcings

Section 4 shows that the ENSO modulation of the QBO period can be simulated by each of the AMIP–OMA–SP, AMIP–OMA–AP, and Coupled–NINT–AP models. The difference in the phase speed of the simulated QBO between ENSO extremes is statistically significant at the 5% significance level for most of those model runs. For Coupled–NINT–SP, one of its historical runs exhibits an opposite response, namely, the simulated QBO propagates downward slower during El Niño than during La Niña while other four runs from the identical model configuration do bring about a faster phase speed of the QBO during warm ENSO events. However, no matter whether the difference in the QBO period simulated by Coupled–NINT–SP is positive or negative between ENSO extremes, it is not statistically significant at the 5% significance level. In this section, we start with investigating how the first three terms in Eq. (7), i.e., the parameterized GW forcing, the resolved wave forcing, and the TEM advection, respond to ENSO extremes and how their evolutions are related with those of the QBO winds simulated by the GISS E2.2 models.

As shown in sections 3 and 4, both the observed and simulated QBO can be very well represented by the trajectory of $\left(PC_1(t), PC_2(t)\right)$ in a linear space spanned by the first two orthonormal EOFs. In other words, at any time t, the QBO wind profile, $U'_{profile}$ is very close to the following linear combination:

543 $PC_1(t) \cdot EOF_1 + PC_2(t) \cdot EOF_2$. Here, the QBO wind, U', refers to the deseasonalized and smoothed
544 monthly mean zonal winds averaged over the zonal belt from 5° S to 5° N. We construct the composite
545 fields of the QBO winds, the GW forcing, the resolved wave forcing, and the TEM advection according
546 to the phase angle of the QBO wind profiles. For each month that falls into the El Niño or La Niña
547 category, we use Eq. (2) to calculate the phase angle of the QBO wind profile, each cycle of which over
548 the 1871–2013 period is divided into 24 bins with the bin size of 15°. Note that if two QBO wind profiles
549 belong in the same bin, they look similar because any one of them can be expressed by the other
550 multiplied by a scalar factor. Therefore, for each of the El Niño and La Niña categories, it is very natural
551 for us to generate the composite QBO winds for that category by averaging all wind profiles in each bin
552 and produce the concomitant composite fields of the GW forcing, the resolved wave forcing, and the
553 TEM advection in the corresponding bin.

554 Fig. 4 depicts the composite fields of the QBO winds (black contours) and parameterized (left panels)
555 and resolved (right panels) wave forcing averaged over all realizations of the Coupled–NINT–AP
556 ensemble. All composite fields in this section have been subjected to the averaging over the latitudinal
557 belt from 5°S to 5°N. The ensemble average is achieved on the basis that the respective vertical
558 structures of the first two leading EOFs are almost identical among all five Coupled–NINT–AP ensemble
559 runs as demonstrated in Fig. 1. Both Figs. 4a and 4b show a characteristic feature of the QBO. Namely,
560 the maximum eastward and westward wave forcing from parameterized GWs are located below and
561 propagate downward with the westerly and easterly QBO jets. Fig. 4c reveals the stronger parameterized
562 GW forcing in both eastward and westward shear zones of the QBO winds during El Niño than during
563 La Niña, which gives rise to the faster phase speed of the QBO during warm ENSO episodes than during
564 its cold counterparts. Figs. 4d and 4e also show that the relationship between resolved wave forcing and
565 the QBO winds are somewhat more complex. When zonal wind anomalies are close to zero, the coherent

and modest resolved westward wave forcing helps the easterly shear zone of the QBO winds to propagate downwards from the 10 hPa level to the 70 hPa level during both the cold and warm ENSO episodes while the coherent and modest resolved eastward wave forcing helps the westerly shear zone of the QBO winds to propagate downwards only from the 20 hPa level to the 70 hPa level during both the cold and warm ENSO episodes. At altitudes above the 20 hPa level, easterly jet cores are modestly weakened by the resolved eastward wave forcing during the two extreme ENSO phases. In particular, Fig. 4f indicates that at altitudes above the 30 hPa level the response of the resolved wave forcing to the ENSO acts to slow down the downward propagation of the QBO during El Niño than during La Niña. However, the parameterized GW forcing shown in Fig. 4 clearly dominates over the resolved wave forcing, which is consistent with the finding of DallaSanta et al. (2021) that the parameterized convective GWs play a dominant role in generating the spontaneous QBO in the GISS E2.2 models.

Figs. 5a–5c depict the composite fields of the QBO winds (black contours) and TEM advection averaged over all realizations of the Coupled–NINT–AP ensemble. Comparing Figs. 5a–5c with Fig. 4 reveals that the TEM advection composite is also larger than composite resolved wave forcing in the Coupled–NINT–AP model. Thus, the QBO simulated by this model is intimately related to the parameterized GW forcing and the TEM advection. It is well-known that while wave forcing is largely balanced out by the TEM advection in the extratropical stratosphere (Haynes, et al., 1991) tropical wave forcing not only drives internal variabilities of zonal winds but also cancel out the TEM advection in the stratosphere (Scott and Haynes, 1998). Figs. 5a–5b also show that the maximum positive and negative advective tendencies are located above rather than below and propagate downward with the westerly and easterly QBO jets, thus acting to slow down the downward propagation of the QBO, which is mainly caused by the persistent tropical upwelling and a general feature of the QBO (Giorgetta et al. 2006; Rind et al., 2014). Fig. 5c indicates that there exist stronger positive and negative advective tendencies above

589 the westerly and easterly QBO jets during El Niño than during La Niña. In other words, the TEM
590 advection alone leads to a slower phase speed of the QBO during El Niño than during La Niña. This is
591 not surprising because El Niño gives rise to a stronger tropical upwelling in the lower stratosphere (Calvo
592 et al., 2010; Simpson et al., 2011; Domeisen et al., 2019).

593 Figs. 5d–5f show the composite the QBO winds (black contours) and the composite sum of
594 parameterized GW forcing, resolved wave forcing, and TEM advection averaged over all realizations of
595 the Coupled–NINT–AP ensemble. In other words, the upper, middle, and lower panels depict the sum
596 of the fields shown in all the corresponding panels of Figure 5 and Figs. 5a–5c. The pattern of the
597 composite sum is generally determined by the pattern of parameterized GW forcing even though the
598 latter is more coherent than the former. Thus, we conclude that the shorter QBO period during El Niño
599 simulated by Coupled–NINT–AP is mainly caused by stronger parameterized GW forcing during warm
600 ENSO episodes. We also find that stronger parameterized GW forcing during warm ENSO events are
601 simulated by AMIP–OMA–SP and AMIP–OMA–AP models (figures not shown), which helps us
602 understand why most members from each of those three ensembles generate a spontaneous QBO whose
603 phase speed is statistically significantly greater during El Niño than during La Niña at the 5%
604 significance level.

605 Now we explore how ENSO influences parameterized GW forcing, resolved wave forcing, and TEM
606 advection simulated by the Coupled–NINT–SP model, i.e., the remaining model listed in Tables 1 and
607 2. Contrasting between Fig. 6a and Fig. 4c reveals that the ensemble mean composite response to the
608 ENSO of parameterized GW forcing simulated by Coupled–NINT–SP is substantially weaker than that
609 simulated by Coupled–NINT–AP. Although the Coupled–NINT–SP simulations still bring about
610 enhanced westward parameterized GW forcing in the easterly shear zones of the simulated QBO winds
611 during El Niño in contrast to La Niña, the magnitude of the reinforcement is only about two thirds of

612 that simulated by Coupled–NINT–AP. In particular, in Fig. 6a there is no coherent pattern of enhanced
613 eastward parameterized GW forcing in the westerly shear zones of the QBO winds simulated by
614 Coupled–NINT–SP, which is in glaring contrast to the coherent pattern of positive enhancement shown
615 in Fig. 4c generated from the Coupled–NINT–AP ensemble. Figs. 6b and 6c show that both resolved
616 wave forcing and TEM advection respond to the ENSO weakly and uniformly in the Coupled–NINT–
617 SP ensemble simulations. Combining all three composite fields together, Fig. 6d demonstrates that the
618 ensemble mean of the Coupled–NINT–SP simulations still simulates a coherent but much weaker
619 response to the ENSO of resultant forcing at altitudes above the 40 hPa level, which helps us to explain
620 why only some of the Coupled–NINT–SP ensemble runs can simulate a faster QBO descent rate during
621 El Niño than during La Niña and the ENSO does not make a difference in the phase speed of the QBO
622 that is statistically significant at the 5% significance level in any of those Coupled–NINT–SP runs.

623 **5.2 ENSO modulation of the generation and propagation of parameterized gravity waves**

624 A natural question that arises is how the parameterized GW forcing relates to the SST anomalies of
625 ENSO extremes specified in or simulated by the GISS E2.2 models listed in Table 1. Figs. 7a and 7b
626 show the ensemble averages of the composite SST anomalies averaged over all La Niña and El Niño
627 months respectively over the 1871–2013 period simulated by Coupled–NINT–AP. Comparing Figs. 7a
628 and 7b with Figs. 3a and 3b reveals that the amplitude of the ENSO simulated by Coupled–NINT–AP is
629 larger than the observed. Figs. 7c and 7d show that the differences between the simulated SST anomalies
630 arising from the ENSO events shown in Figs. 7a and 7b and the observed ones shown in Figs. 3a and 3b,
631 indicating that the largest discrepancies occur over the western and eastern equatorial Pacific. Figs. 7a
632 and 7b also demonstrate that the model has a capability to simulate the ENSO amplitude asymmetry
633 (Cane and Zebiak, 1987; Yu and Mechoso, 2001), namely, the amplitudes of the ENSO are relatively
634 larger during warm episodes than during cold episodes. As in Fig. 3 of Zhao and Sun (2022), Fig. 7e

depicts the sum of the composite SST anomalies shown in Figs. 7a and 7b that they used to characterize the ENSO amplitude asymmetry while Fig. 7f shows their difference. Their Fig. 3 reveals that most CMIP6 models cannot simulate the pattern of a positive residual in the sum of the composites of ENSO extremes in the tropical eastern Pacific. Further comparison between Fig. 3 in Zhao and Sun (2022) and Fig. 7e indicates that the ENSO amplitude asymmetry simulated by Coupled–NINT–AP is only about 50% of that simulated by the GISS-E2-1-H model discussed in their study whose ENSO amplitude asymmetry is comparable to the observed.

Since this study is chiefly concerned with the ENSO modulation of the QBO period, we focus on the ensemble mean difference between the composite SST anomalies of ENSO extremes, which can be interpreted as the trough-to-crest amplitude of the ENSO cycle. Comparing Fig. 8a with Fig. 3c indicates that the trough-to-crest ENSO amplitude derived from the HadISST1 dataset over the 1871–2013 period is somewhat smaller than that derived from the ERSSTv5 dataset over the 1953–2015 period, which is consistent with the finding by Grothe et al. (2019) that the increase in the ENSO variability is statistically significant (>95% confidence) from the preindustrial to recent era, no matter whether the latter is defined by the previous 30, 50, 75, or 100 years before 2016. Fig. 7f and Fig. 8 also reveal that the ENSO amplitude simulated by Coupled–NINT–AP is substantially greater than that simulated by Coupled–NINT–SP, which was previously revealed in Rind et al. (2020). The tendency to generate stronger ENSO oscillations means that the Coupled-NINT-AP runs will also more readily exceed the $\pm 0.5°C$ criteria for El Nino and La Nina events, and the Coupled–NINT–AP runs do simulate more ENSO events over the 1871–2013 period than the Coupled–NINT–SP runs as indicated in subsection 2.3.1. Fig. 8 further shows that the ENSO amplitude simulated by Coupled–NINT–SP is noticeably greater than that specified in the AMIP–OMA–SP and AMIP–OMA–AP models (which being derived from observations, are the same) even though it is substantially weaker than that simulated by Coupled–NINT–AP.

We also ascertain that the Hadley circulation simulated by each of the four models listed in Table 1 strengthens and weakens during warm and cold ENSO episodes respectively, which is consistent with the finding by Oort and Yienger (1996). Consistent with the simulated ENSO amplitudes, the response of the Hadley circulation to ENSO extremes simulated by Coupled–NINT–AP is substantially stronger than that simulated by Coupled–NINT–SP, which is in turn stronger than the those from two AMIP models whose responses to ENSO extremes are comparable (figures not shown).

Schirber (2015) discovered that the parameterized GW mean momentum source is about 15% larger in the El Niño ensemble than in the La Niña ensemble because the El Niño leads to enhanced precipitation and convective heating. Similarly, we calculate the absolute value of convective momentum fluxes (ACMF) at the source altitude and composite the ACMF anomalies averaged over the latitudinal belt between 5°S and 5°N from El Niño and La Niña categories respectively over the 1871–2013 period. Fig. 9 shows the composite difference in the equatorial mean ACMF anomalies between El Niño and La Niña over the 1871–2013 period, indicating that the absolute momentum fluxes at the source levels over the equatorial best is larger during El Niño episodes than during La Niña episodes for each of 19 runs listed in Table 1. This finding is consistent with that of Geller et al. (2016b), Alexander et al. (2017), and Kang et al. (2018), namely, both convective GW momentum fluxes and convective GW wave forcing are generally stronger during El Niño than during La Niña in the equatorial region. The ensemble mean difference in the absolute momentum fluxes at the source levels averaged over that equatorial belt between El Niño and La Niña is obtained as 0.07, 0.15, 0.10, and 0.12 mPa for AMIP–OMA–SP, AMIP–OMA–AP, Coupled–NINT–SP, and Coupled–NINT–AP, respectively. Note that these composite differences in ACMF between El Nino and La Nina translate into ACMF being about 10-20% larger in the El Niño ensembles than in the La Niña ensembles, thus agree with the Schirber (2015). Since the QBO period is inversely dependent upon the momentum flux (Plumb, 1977), the

differences in equatorial absolute momentum fluxes at the source altitude contribute to shortening and lengthening of the simulated QBO period during warm and cold ENSO phases, respectively.

Fig. 3 shows that the locations of warmest SSTs shift from the maritime continent during La Niña episodes to the central and eastern equatorial Pacific during El Niño episodes. Since strong convective activities over tropical oceans are generally located above the regions where the SSTs exceed $26°-28°$ C (Graham and Barnett, 1987; Zhang, 1993), strong convective activities also shift eastward from cold to warm ENSO phases, as illustrated in Fig. 2. Using satellite data, the climatological study by Sullivan et al. (2019) demonstrated that the occurrence of organized deep convection during El Niño events increases threefold in the central and eastern Pacific and decreases twofold outside of these regions in contrast to that during La Niña events. It is well-established that the Walker circulation strengthens during La Niña and weakens during El Niño (Bjerknes, 1969).

Next, we construct the equatorial zonal winds as the zonal winds averaged from 5°S to 5°N. Then we define the equatorial winds during La Niña and El Niño as the equatorial winds averaged over all months that fall into the La Niña and El Niño categories, respectively. Fig. 10 illuminates that the Walker circulation derived from ERA5 reanalysis during El Niño is substantially weaker than its counterpart during La Niña over the equatorial Pacific and the eastern equatorial Indian ocean. Particularly in the upper equatorial troposphere, the westerlies above the central and eastern Pacific during El Niño episodes are decreased by more than 50% as compared with those during La Niña ones while the easterlies above the equatorial Indian ocean and the maritime continent during El Niño conditions are weakened by more than 30% as compared with those during La Niña ones. Kawatani et al. (2019) argue that the weaker upper tropospheric winds during El Niño episodes enable a greater amount of GW momentum fluxes to be transferred from the troposphere into stratosphere because less GWs are filtered out. This argument assumes critical-level absorption of otherwise weakly damped, vertically propagating

GWs, which was adopted by Lindzen and Holton (1968). The weaker Walker circulation leads to a shorter QBO period during El Niño while the stronger Walker circulation results in a longer QBO period during La Niña.

Fig. 11 depicts the ensemble mean composite difference in the equatorial zonal wind anomalies between warm and cold ENSO extremes simulated by the E2.2 models listed in Table 1. The patterns of the simulated wind anomalies shown in Fig. 11 are very similar to that derived from the ERA5 reanalysis shown in Fig. 10c. Namely, the weakened Walker circulation simulated by the E2.2 models during El Niño episodes results in weaker upper tropospheric westerlies over the central and eastern equatorial Pacific and weaker upper tropospheric easterlies over the maritime continent and equatorial Indian ocean while the intensified Walker circulation simulated by the E2.2 models during La Niña episodes leads to stronger upper tropospheric westerlies over the central and eastern equatorial Pacific and stronger upper tropospheric easterlies over the maritime continent and equatorial Indian ocean. The difference in the wind filtering of upward propagating GWs causes a greater transfer of GW momentum fluxes into the tropical stratosphere during El Niño episodes than during La Niña episodes, leading to a shorter QBO period during El Niño events than during La Niña events. Fig. 11 reveals that the maximum contrast in the upper tropospheric zonal winds between warm and cold ENSO extremes simulated by two AMIP models, i.e., AMIP–OMA–SP and AMIP–OMA–AP, reaches -13.1 ms^{-1} and -12.1 ms^{-1}, respectively, over the central and eastern equatorial Pacific, and attains 6.6 ms^{-1} and 6.4 ms^{-1}, respectively, over the maritime continent and equatorial Indian ocean. Those maximum contrasts are somewhat smaller than what is derived from the ERA5 reanalysis shown in Fig.11, namely -15.0 ms^{-1} over the central and eastern equatorial Pacific and 7.8 ms^{-1} over the maritime continent and equatorial Indian ocean. However, the maximum contrast in the upper-tropospheric zonal winds over the central and eastern equatorial Pacific between warm and cold ENSO extremes simulated by two coupled ocean-atmosphere

727 models, i.e., Coupled–NINT–SP and Coupled–NINT–AP, only reaches -7.5 ms^{-1} and -8.2 ms^{-1},
728 respectively, thus is substantially smaller than that derived from the ERA5 reanalysis. Meanwhile, the
729 maximum contrast in the upper-tropospheric zonal winds over the maritime continent and equatorial
730 Indian ocean between warm and cold ENSO extremes simulated by those two coupled models, reaches
731 7.0 ms^{-1} and 10.3 ms^{-1}, respectively, which is slightly smaller than and somewhat larger than the
732 observed values, respectively.

733 While the comparison of the observed and simulated changes in the Walker circulation between warm
734 and cold ENSO extremes shown in Figs. 10 and 11 can account for a shorter QBO period simulated by
735 all GISS E2.2 models and can also explain why the two AMIP models can better capture the ENSO
736 modulation of the QBO period than the Coupled–NINT–SP model as indicated in Table 2, it can neither
737 explain why the Coupled–NINT–AP model can capture the ENSO modulation of the QBO period as two
738 AMIP models nor can illuminate why the coupled model with the altered physics (i.e., Coupled–NINT–
739 AP) performs better than the coupled model with the standard physics (i.e., Coupled–NINT–SP).
740 However, further comparing the simulated SST changes between warm and cold ENSO extremes shown
741 in Figs. 7 and 8 hints that the unduly amplified ENSO in the coupled AP runs holds the key to those
742 unsettled issues that is detailed as follows.

743 Using a large ensemble of multiple climate models, Serva et al. (2020) discovered that the AMIP
744 historical runs generally better capture the ENSO modulation of the QBO period than the coupled ocean-
745 atmosphere historical simulations. In particular, among a few coupled ocean-atmosphere models that do,
746 to various extents, capture the ENSO modulation of the QBO period, the common feature is that each of
747 them can largely simulate the observed OLR anomaly pattern shown in Fig. 2c albeit the magnitudes of
748 those simulated OLR anomalies from their historical runs are roughly 50% stronger than the observed
749 (for more details, refer to their Fig. 8 in Serva et al., 2020). For the sake of comparison, we construct the

750 ensemble mean composite difference in the OLR anomalies between warm and cold ENSO extremes in
751 the same way we constructed the ensemble mean composite difference in the zonal wind anomalies
752 depicted in Fig. 11.

753 Figs. 12a and 12b show that the patterns of the OLR anomalies simulated by AMIP–OMA–SP and
754 AMIP–OMA–AP largely resemble the observed one shown in Fig. 2c. Although the pattern simulated
755 by AMIP–OMA–AP matches better with the observed, the convective activities during El Niño episodes
756 simulated by AMIP–OMA–SP and AMIP–OMA–AP are apparently inadequate over the region where
757 the upper tropospheric westerlies weaken most conspicuously during warm ENSO extremes shown in
758 Figs. 11a and 11b, respectively. Thus, although the contrast in the wind filtering of GWs between El
759 Niño and La Niña episodes simulated by the two AMIP E2.2 models are comparable to the observed,
760 the difference in the GW momentum flux transferred into the equatorial stratosphere between warm and
761 cold ENSO extremes may be smaller than the observed with the correct SSTs. This partly explains why
762 the contrast between the observed mean QBO period during El Niño episodes (i.e., 25.6 months) and the
763 observed mean QBO period during La Niña episodes (i.e., 34.3 months) is higher than that simulated by
764 the two AMIP models shown in Table 2 (i.e., E1 and E2 in Table 2). As exhibited by the coupled model
765 capable of simulating the ENSO modulation of the QBO period, Fig. 12d shows that the contrast in the
766 OLR anomalies between warm and cold ENSO extremes simulated by Coupled–NINT–AP is apparently
767 sharper than the observed one shown in Fig. 2c. In particular, the tropical convection in the central and
768 eastern Pacific during El Niño episodes simulated by Coupled–NINT–AP is both more extensive and
769 more intensive than that simulated by the two AMIP models shown in Figs. 12a and 12b, which is
770 consistent with the fact that the composite contrast in the SST anomalies simulated by Coupled–NINT–
771 AP shown in Fig. 7d is substantially sharper than that prescribed in the two AMIP models shown in Fig.
772 8a. Thus, even though the wind filtering of GWs during El Niño episodes simulated by Coupled–NINT–

AP shown in Figs 12d is significantly smaller than that simulated by AMIP–OMA–SP and AMIP–OMA–AP shown in Figs 12a and 12b, respectively, the combined effect of the lower contrast in the wind filtering and the higher contrast in the amount of GW momentum fluxes generated by convective activities between warm and cold ENSO extremes over the central and eastern tropical Pacific results in a comparable ENSO modulation of the QBO period simulated by Coupled–NINT–AP to that simulated by the two AMIP models as illustrated in Table 2.

Finally, comparing Fig. 12c with Fig. 2c and other three panels in Fig. 12 reveals that convective activities during the warm ENSO phase simulated by the Coupled–NINT–SP model are substantially weaker than both the observed and those simulated by other three models list in Table 1. Combining the small composite OLR difference shown in Fig. 12c and the small difference in the wind filtering shown in Fig. 8c between warm and cold ENSO extremes over the central and eastern equatorial Pacific results in a low contrast in GW forcing between warm and cold ENSO phases shown in Fig. 6a, which, short of the compensating effect of the excessively amplified ENSO in Coupled–NINT–AP ensemble runs, should lead to a relatively weaker ENSO modulation of the QBO period simulated by the Coupled–NINT–SP model as illustrated in Table 2. However, this is not the whole story; and we will return to this subject in the discussion section.

5. Discussion and Conclusions

Both Kawatani et al. (2019) and Serva et al. (2020) pointed out that a relatively high horizontal resolution is necessary to simulate the ENSO modulation of the QBO period. Employing an Earth system model with T42 (~2.79°) horizontal resolution, Kawatani et al. (2019) further demonstrated that the ENSO modulation of the QBO could not be simulated with their fixed GW sources. Serva et al. (2020)

795 also pointed out that the reliance on stationary parameterizations of GWs is partly responsible for failing
796 to simulate the observed modulation of the QBO by the ENSO in current climate models.

797 Rind et al. (1988) implemented various interactive GW sources in the GISS climate models. With the
798 momentum flux of the parameterized convective waves dependent on the convective mass flux,
799 buoyancy frequency and density at the top of the convective region, wind velocity averaged over the
800 convective layers, etc. and with a horizontal resolution of 2° latitude by 2.5° longitude, all the four
801 versions of GISS E2.2 models in this study can simulate the ENSO modulation of the QBO period to
802 various degrees. For each of 19 runs conducted in this study, the absolute momentum fluxes at the source
803 levels over the equatorial belt is larger during El Niño episodes than during La Niña episodes, leading
804 to a shorter and longer QBO period, respectively.

805 Realistic simulation of the ENSO modulation of the QBO periods entails the realistic simulation of
806 both the ENSO and the QBO. With the realistic SSTs specified, both the composite difference in the
807 Walker circulation and the composite OLR difference between warm and cold ENSO extremes simulated
808 by the two AMIP E2.2 models are close to the observed. Since the AMIP model with the "altered physics"
809 performs better than that with the "standard physics" as far as the simulated OLR is concerned, the
810 ensemble mean difference in the QBO period between La Niña and El Niño episodes (i.e., ~4.5 months)
811 simulated by AMIP–OMA–AP is larger than that simulated by AMIP–OMA–SP (i.e., ~3.9 months),
812 which indicates that convective parameterization scheme is important not only for simulating the
813 resolved waves as pointed out by Horinouchi et al. (2003) and Lott et al. (2014), but also for
814 parameterizing GWs. However, the convective activities simulated by both AMIP E2.2 models are still
815 inadequate over the central and eastern equatorial Pacific as compared to the observed, which may partly
816 account for why the ensemble mean differences in the QBO period between La Niña and El Niño
817 episodes simulated by both AMIP models are smaller than the observed difference (i.e., ~8.7 months).

Although the simulated Walker circulations associated with the ENSO cycle are comparable among the two coupled ocean-atmosphere models in this study, the E2.2 model with the "standard physics" performs well in its simulated SSTs which is very close to the observed while the ENSO amplitudes simulated by other model with the "altered physics" are substantially greater than the observed. Yet the model with the "standard physics" not only fails to properly simulate the shift of the strongest convection from the maritime continent during La Niña to the central and eastern equatorial Pacific during El Niño, but also grossly fail to simulate the sufficient amplitude of the OLR concomitant with the ENSO cycle. The weaker response of the Walker circulation and convective activities to the ENSO cycle together with the dislocated centers of convection concomitant to cold and warm ENSO extremes leads to the smallest ensemble mean difference in the QBO period between La Niña and El Niño episodes (i.e., ~2.7 months) simulated by the Coupled–NINT–SP model. The weaker variation of the Walker circulation and the excessive change in convection compensate to give an impression of realistically simulating the ENSO modulation of the QBO period by the other model with the "altered physics", i.e., Coupled–NINT–AP, with its ensemble mean differences in the QBO period between La Niña and El Niño episodes being ~4.8 months. However, it is worth pointing out that we don't regard that model as the best among the four models listed in Table 1 because the relatively satisfactory results are achieved in a compensatory, thus unrealistic, way. Serva et al. (2020) conducted both the atmosphere-only and coupled historical simulations and found that the trough-to-crest amplitudes of the OLR associated with the ENSO cycle are two times larger than the observed for a few models that relatively well capture the ENSO modulation of the QBO period, which together with our results suggests that the parameterized convection is a linchpin of realistically simulating the ENSO, the QBO, and the ENSO modulation of the QBO.

840 Intriguingly, the simulated difference in the QBO period between La Niña and El Niño is 6.2 months
841 from the first realization simulated by Coupled–NINT–SP. However, it is not statistically significant at
842 the 5% significance level. Meanwhile, the differences in the QBO period between La Niña and El Niño
843 from most of the realizations simulated by Coupled–NINT–AP are apparently less than 6.2 months but
844 are all statistically significant. To gain a deeper insight, we calculate the frequency power spectra of
845 standardized ONIs derived from the observed and simulated SSTs. Fig. 13a depicts the power spectral
846 densities (PSD) of standardized ONI between 1953 and 2015 derived from the NOAA ERSSTv5 SST
847 while Fig. 13b delineates the PSD of standardized ONI between 1871 and 2013 derived from the
848 HadISST1 dataset as used in the AMIP runs. Figs. 13a and 13b show that although the ENSO accounts
849 for the lion's share of SST variabilities, there is a good amount of SST variabilities on the decadal and
850 multidecadal time scales. Fig. 13d illustrates the PSD of standardized ONI between 1871 and 2013
851 simulated by the second realization of Coupled–NINT–AP, which demonstrates that the ENSO
852 overwhelmingly dominates over any other noises in SST variabilities simulated by those E2.2 models
853 with the "altered physics". Furthermore, Fig. 13c shows the PSD of standardized ONI between 1871 and
854 2013 simulated by the first realization of Coupled–NINT–SP. Apparently, the SST variabilities
855 simulated by the E2.2 model with the "standard physics" are comparable to the observed, thus more
856 realistic. The smaller ratio of the ENSO signal to the noise simulated by the first realization of Coupled–
857 NINT–SP and the much larger ratio simulated by the second realizations of the E2.2 models with "alter
858 physics" explain why the difference of 6.2 months in the QBO period between La Niña and El Niño
859 from the former is not statistically significant while why the differences of 2.6 and 4.8 months from the
860 latter are statistically significant as shown in Table 2.

861 The rich spectrum of internal variabilities simulated by Coupled–NINT–SP, to a large degree, reflects
862 the observed ones shown in Figs. 13a and13b. Those large internal variabilities likely underlie why one

of the historical runs simulated by Coupled–NINT–SP gives rise to a slower mean QBO phase speed during El Niño than during La Niña while other four runs from Coupled–NINT–SP do simulate a faster phase speed of the QBO during warm ENSO events. Kawatani et al. (2019) conducted two 100-yr experiments: one for a perpetual El Niño condition and the other for a perpetual La Niña condition. Their Fig. 3 shows that although the long-term mean QBO period from the El Niño run is shorter than that from the La Niña run, this is not the case for each individual year. This is because various internal variabilities exert their influence over the QBO period.

None of the E2.2 configurations robustly simulate an ENSO modulation of QBO amplitude, consistent with the weaker signal present in observations (Yuan et al., 2014). It is not surprising because our observational analyses show that the ENSO modulation of the QBO amplitude is not statistically significant at the 95% confidence level. In order to realistically simulate the ENSO modulation of the QBO, various aspects of climate models such as the SSTs, the Walker circulations, the parameterizations of convection and GWs need to be further improved, which is fortunately ongoing under the auspices of the SPARC Quasi-Biennial Oscillation initiative (Butchart et al., 2018).

Data availability

The monthly mean zonal winds from Free University of Berlin are obtained from https://www.geo.fu-berlin.de/en/met/ag/strat/produkte/qbo/index.html. The NOAA ERSSTv5 SST is acquired from https://www.ncei.noaa.gov/products/extended-reconstructed-sst. The NCEI OLR is downloaded from https://www.ncei.noaa.gov/products/climate-data-records/outgoing-longwave-radiation-monthly. The ERA5 monthly mean zonal winds are obtained from the ECMWF C3S at Climate Data Store: https://cds.climate.copernicus.eu/. The GISS ModelE E2.2 data are available from the Earth System Grid

Federation and also from the NASA Center for Climate Simulation data portal (including non-CMIP6 simulations).

Author contributions

All authors made equal contributions to this work.

Competing interests

The authors declare that they have no conflict of interest.

Acknowledgements: Climate modeling at GISS is supported by the NASA Modeling, Analysis and Prediction program, and resources supporting this work were provided by the NASA High-End Computing (HEC) Program through the NASA Center for Climate Simulation (NCCS) at Goddard Space Flight Center. The authors thank three anonymous reviewers for their constructive comments, which led to a significantly improved paper

References

Alexander, M. J., Ortland, D. A., Grimsdell, A. W., and Kim, J.-E.: Sensitivity of Gravity Wave Fluxes to Interannual Variations in Tropical Convection and Zonal Wind, J. Atmos. Sci., 74, 2701–2716, https://doi.org/10.1175/JAS-D-17-0044.1, 2017.

Andrews, D. G., Mahlman, J. D., and Sinclair, R. W.: Eliassen–Palm diagnostics of wave-mean flow interaction in the GFDL" SKYHI" general circulation model, J. Atmos. Sci., 40, 2768–2784, https://doi.org/10.1175/1520-0469(1983)040%3C2768:ETWATM%3E2.0.CO;2, 1983.

907 Andrews, D. G., Holton, J. R., and Leovy, C. B.: Middle Atmosphere Dynamics, Academic Press, 489
908 pp, 1987.
909 Angell, J. K.: On the variation in period and amplitude of the quasi-biennial oscillation in the equatorial
910 stratosphere, 1951–85, Mon. Weather Rev., 114, 2272–2278, https://doi.org/10.1175/1520-
911 0493(1986)114%3C2272:OTVIPA%3E2.0.CO;2, 1986.
912 Anstey, J. A., Banyard, T. P., Butchart, N., Coy, L., Newman, P. A., Osprey, S., and Wright, C. J.:
913 Prospect of Increased Disruption to the QBO in a Changing Climate, Geophys. Res. Lett., 48,
914 e2021GL093058, https://doi.org/10.1029/2021GL093058, 2021.
915 Baldwin, M. P., Gray, L. J., Dunkerton, T. J., Hamilton, K., Haynes, P. H., Randel, W. J., Holton, J. R.,
916 Alexander, M. J., Hirota, I., Horinouchi, T., Jones, D. B. A., Kinnersley, J. S., Marquardt, C., Sato,
917 K., and Takahashi, M.: The Quasi-biennial oscillation, Rev. Geophys., 39, 179–229,
918 https://doi.org/10.1029/1999RG000073, 2001.
919 Bauer, S. E., Tsigaridis, K., Faluvegi, G., Kelley, M., Lo, K. K., Miller, R. L., Nazarenko, L., Schmidt,
920 G. A., and Wu, J.: Historical (1850–2014) Aerosol Evolution and Role on Climate Forcing Using
921 the GISS ModelE2.1 Contribution to CMIP6, J. Adv. Model. Earth Sy., 12, e2019MS001978,
922 https://doi.org/10.1029/2019ms001978, 2020.
923 Bergman, J. W. and Salby, M. L.: Equatorial wave activity derived from fluctuations in observed
924 convection, J. Atmos. Sci. 51, 3791–3806, https://doi.org/10.1175/1520-
925 0469(1994)051%3C3791:EWADFF%3E2.0.CO;2, 1994.
926 Bjerknes, J.: Atmospheric teleconnections from the equatorial Pacific, Mon. Weather Rev., 97, 163–172,
927 https://doi.org/10.1175/1520-0493(1969)097%3C0163:ATFTEP%3E2.3.CO;2, 1969.
928 Bushell, A. C., Anstey, J. A., Butchart, N., Kawatani, Y., Osprey, S. M., Richter, J. H., Serva, F.,
929 Braesicke, P., Cagnazzo, C., Chen, C.-C., Chun, H.-Y., Garcia, R. R., Gray, L. J., Hamilton, K.,

Kerzenmacher, T., Kim, Y.-H., Lott, F., McLandress, C., Naoe, H., Scinocca, J., Smith, A. K., Stockdale, T. N., Versick, S., Watanabe, S., Yoshida, K., and Yukimoto, S.: Evaluation of the Quasi-Biennial Oscillation in global climate models for the SPARC QBO-initiative, Q. J. Roy. Meteor. Soc., 1–31, https://doi.org/10.1002/qj.3765, 2020.

Butchart, N., Anstey, J., Hamilton, K., Osprey, S., McLandress, C., Bushell, A. C., Kawatani, Y., Kim, Y.-H., Lott, F., Scinocca, J., Stockdale, T.N., Andrews, M., Bellprat, O., Braesicke, P., Cagnazzo, C., Chen, C.-C., Chun, H.-Y., Dobrynin, M., Garcia, R., Garcia-Serrano, J., Gray, L.J., Holt, L., Kerzenmacher, T., Naoe, H., Pohlmann, H., Richter, J. H., Scaife, A.A., Schenzinger, V., Serva, F., Versick, S., Watanabe, S., Yoshida, K. and Yukimoto, S.: Overview of experiment design and comparison of models participating in phase 1 of the SPARC Quasi-Biennial Oscillation initiative (QBOi), Geoscientific Model Development, 11, 1009–1032. https://doi.org/10.5194/gmd-11-1009-2018, 2018.

Calvo, N., Garcia, R. R., Randel, W. J., and Marsh, D. R.: Dynamical mechanism for the increase in tropical upwelling in the lowermost tropical stratosphere during warm ENSO events, J. Atmos. Sci., 67, 2331–2340, https://doi.org/10.1175/2010JAS3433.1, 2010.

Cane, M. and Zebiak, S. E.: Prediction of El Niño events using a physical model, in Atmospheric and Oceanic Variability, edited by H. Cattle, Royal Meteorological Society Press, London, 153-182, 1987.

Chernick, M. R.: Bootstrap methods: A guide for practitioners and researchers, Wiley-Interscience, 369pp, 2007).

Christiansen, B., Yang, S., and Madsen, M. S.: Do strong warm ENSO events control the phase of the stratospheric QBO?, Geophys. Res. Lett., 43, 10489–10495, https://doi.org/10.1002/2016GL070751, 2016.

Collimore, C. C., Martin, D. W., Hitchman, M. H., Huesmann, A., and Waliser, D. E.: On the relationship between the QBO and tropical deep convection, J. Climate, 16, 2552–2568, https://doi.org/10.1175/1520-0442(2003)016%3C2552:OTRBTQ%3E2.0.CO;2, 2003.

Coy, L., Newman, P. A., Strahan, S., and Pawson, S.: Seasonal variation of the quasi-biennial oscillation descent, J. Geophys. Res.-Atmos., 125, e2020JD033077, https://doi.org/10.1029/2020JD033077, 2020.

DallaSanta, K., Orbe, C., Rind, D., Nazarenko, L., and Jonas, J.: Dynamical and trace gas responses of the Quasi-Biennial Oscillation to increased CO_2, J. Geophys. Res. Atmos., 126, e2020JD034151. https://doi.org/10.1029/2020JD034151, 2021.

Domeisen, D. I. V., Garfinkel, C. I., and Butler, A. H.: The Teleconnection of El Niño Southern Oscillation to the Stratosphere, Rev. Geophys., 57, 5–47, https://doi.org/10.1029/2018RG000596, 2019.

Garfinkel, C. I. and Hartmann, D. L.: Effects of El Nino – South- ern Oscillation and the Quasi-Biennial Oscillation on polar tem- peratures in the stratosphere, J. Geophys. Res., 112, D19112, https://doi.org/10.1029/2007JD008481, 2007.

Garfinkel, C. I. and Hartmann, D. L.: The influence of the quasi-biennial oscillation on the troposphere in winter in a hierarchy of models. Part I: Simplified dry GCMs, J. Atmos. Sci., 68, 1273–1289, https://doi.org/10.1175%2F2011JAS3665.1, 2011a.

Garfinkel, C. I. and Hartmann, D. L.: The influence of the quasi-biennial oscillation on the troposphere in winter in a hierarchy of models. Part II: Perpetual winter WACCM runs, J. Atmos. Sci., 68, 2026–2041, https://doi.org/10.1175%2F2011JAS3702.1, 2011b.

Geller, M. A., Zhou, T., Shindell, D., Ruedy, R., Aleinov, I., Nazarenko, L., Tausnev, N. L., Kelley, M., Sun, S., Cheng, Y., Field, R. D., and Faluvegi, G.: Modeling the QBO-improvements resulting from

higher-model vertical resolution, J. Adv. Model. Earth Syst., 8, 1092–1105, https://doi.org/10.1002/2016MS000699, 2016a.

Geller, M. A., Zhou, T., and Yuan, W.: The QBO, gravity waves forced by tropical convection, and ENSO, J. Geophys. Res. Atmos., 121, 8886-8895, https://doi.org/10.1002/2015JD024125, 2016b.

Giorgetta, M. A., Bengtson, L., and Arpe, K.: An investigation of QBO signals in the east Asian and Indian monsoon in GCM experiments, Climate Dynamics, 15, 435–450, https://doi.org/10.1007/s003820050292, 1999.

Giorgetta, M. A., Manzini, E., and Roeckner, E., Esch, M., and Bengtsson, L.: Climatology and forcing of the quasi-biennial oscillation in the MAECHEM5 model, J. Climate, 19, 3882–3901, https://doi.org/10.1175/JCLI3830.1, 2006.

Graham, N. E. and Barnett, T. P.: Sea surface temperature, surface wind divergence, and convection over tropical oceans, Science, 238, 657–659, https://doi.org/10.1126/science.238.4827.657, 1987.

Gray, W. M.: Atlantic seasonal hurricane frequency. Part I: El Niño and 30-mb quasi-biennial oscillation influences, Mon. Wea. Rev., 112, 1649–1688, https://doi.org/10.1175/1520-0493(1984)112%3C1649:ASHFPI%3E2.0.CO;2, 1984.

Gray, W. M., Sheaffer, J. D., and Knaff, J.: Influence of the stratospheric QBO on ENSO variability, J. Meteor. Soc. Jpn., 70, 975–995, https://doi.org/10.2151/jmsj1965.70.5_975, 1992.

Grothe, P. R., Cobb, K. M., Liguori, G., Di Lorenzo, E., Capotondi, A., Lu, Y., Cheng, H., Edwards, R.L., Southon, J. R., Santos, G. M., Deocampo, D. M., Lynch-Stieglitz, J., Chen, T., Sayani, H. R., Thompson, D. M., Conroy, J. L., Moore, A. L., Townsend, K., Hagos, M., O'Connor, G., and Toth, L. T.: Enhanced El Niño–Southern oscillation variability in recent decades, Geophys. Res. Lett., 47, e2019GL083906, https://doi.org/10.1029/2019GL083906, 2019.

998 Hamilton, K., Osprey, S., and Butchart, N.: Modeling the stratosphere's "heartbeat," Eos, 96, p. 8,
999 https://doi.org/10.1029/2015EO032301, 2015.
1000 Hamilton, K., Hertzog, A., Vial, F., and Stenchikov, G.: Longitudinal variation of the stratospheric Quasi-
1001 Biennial Oscillation, J. Atmos. Sci., 61, 383–402, https://doi.org/10.1175/1520-
1002 0469(2004)061%3C0383:LVOTSQ%3E2.0.CO;2, 2004.
1003 Hansen, F., Matthes, K., and Wahl, S.: Tropospheric QBO–ENSO interactions and differences between
1004 the Atlantic and Pacific, J. Climate, 29, 1353–1368, https://doi.org/10.1175/JCLI-D-15-0164.1,
1005 2016
1006 Hasebe, F.: Quasi-biennial oscillations of ozone and diabatic circulation in the equatorial stratosphere, J.
1007 Atmos. Sci., 51, 729–745, https://doi.org/10.1175/1520-
1008 0469(1994)051%3c0729:QBOOOA%3e2.0.CO;2, 1994.
1009 Haynes, P. H., McIntyre, M. E., Shepherd, T. G., Marks, C. J., and Shine, K. P.: On the "Downward
1010 Control" of Extratropical Diabatic Circulations by Eddy-Induced Mean Zonal Forces, J. Atmos. Sci.,
1011 48, 651–678, https://doi.org/10.1175/1520-0469(1991)048%3C0651:OTCOED%3E2.0.CO;2, 1991.
1012 Hersbach, H., Bell, B., Berrisford, P., Hirahara, S., Horányi, A., Muñoz-Sabater, J., Nicolas, J., Peubey,
1013 C., Radu, R., Schepers, D., Simmons, A., Soci, C., Abdalla, S., Abellan, X., Balsamo, G., Bechtold,
1014 P., Biavati, G., Bidlot, J., Bonavita, M., Chiara, G., Dahlgren, P., Dee, D., Diamantakis, M., Dragani,
1015 R., Flemming, J., Forbes, R., Fuentes, M., Geer, A., Haimberger, L., Healy, S., Hogan, R. J., Hólm,
1016 E., Janisková, M., Keeley, S., Laloyaux, P., Lopez, P., Lupu, C., Radnoti, G., Rosnay, P., Rozum, I.,
1017 Vamborg, F., Villaume, S., and Thépaut, J.-N.: The ERA5 global reanalysis, Q. J. Roy. Meteor. Soc.,
1018 online first, https://doi.org/10.1002/qj.3803, 2020.

1019 Hitchman, M. H., and Huesmann, A. S.: Seasonal influence of the quasi-biennial oscillation on
1020 stratospheric jets and Rossby wave breaking, J. Atmos. Sci., 66, 935–946,
1021 https://doi.org/10.1175%2F2008JAS2631.1, 2009.
1022 Ho, C.-H., Kim, H.-S., Jeong, J.-H., and Son, S.-W.: Influence of stratospheric quasi-biennial oscillation
1023 on tropical cyclone tracks in the western North Pacific, Geophys. Res. Lett., 36, L06702,
1024 http://dx.doi.org/10.1029/2009GL037163, 2009.
1025 Holton, J.: Waves in the equatorial stratospheric generated by tropospheric heat resources, J. Atmos. Sci.,
1026 27, 368–375, https://doi.org/10.1175/1520-0469(1972)029%3C0368:WITESG%3E2.0.CO;2, 1972.
1027 Holton, J. R. and Lindzen, R. S.: An updated theory for the quasi-biennial cycle of the tropical
1028 stratosphere, J. Atmos. Sci., 29, 1076–1080, https://doi.org/10.1175/1520-
1029 0469(1972)029%3c1076:AUTFTQ%3e2.0.CO;2, 1972.
1030 Holton, J. R. and Tan, H.: The Influence of the equatorial quasi-biennial oscillation on the global
1031 circulation at 50 mb, J. Atmos. Sci., 37, 2200–2208, https://doi.org/10.1175/1520-
1032 0469(1980)037%3c2200:TIOTEQ%3e2.0.CO;2, 1980.
1033 Horinouchi, T., Pawson, S., Shibata, K., Manzini, E., Giorgetta, M., and Sassi, F.: Tropical cumulus
1034 convection and upward propagating waves in middle-atmospheric GCMs, J. Atmos. Sci., 60, 2765–
1035 2782, https://doi.org/10.1175/1520-0469(2003)060%3C2765:TCCAUW%3E2.0.CO;2, 2003.
1036 Hu, Z.-Z., Huang, B., Kinter, J. L., Wu, Z., and Kumar, A.: Connection of the stratospheric QBO with
1037 global atmospheric general circulation and tropical SST. Part II: Interdecadal variations, Climate
1038 Dynamics, 38, 25–43, https://doi.org/10.1007/s00382-011-1073-6, 2012.
1039 Huang, B. H., Hu, Z. Z., Kinter, J. L., Wu, Z. H., and Kumar, A.: Connection of stratospheric QBO with
1040 global atmospheric general circulation and tropical SST. Part I: Methodology and composite life
1041 cycle, Climate Dynamics, 38, 1–23, https://doi.org/10.1007%2Fs00382-011-1250-7, 2012.

1042 Huang, B., Thorne, P. W., Banzon, V. F., Boyer, T., Chepurin, G., Lawrimore, J. H., Menne M. J., Smith,
1043 T. M., Vose R. S., and Zhang, H. M.: Extended reconstructed sea surface temperature, version 5
1044 (ERSSTv5): upgrades, validations, and intercomparisons, J. Climate, 30, 8179–
1045 8205, https://doi.org/10.1175/JCLI-D-16-0836.1, 2017.
1046 Kang, M.-J., Chun, H.-Y., Kim, Y.-H., Preusse, P., and Ern, M.: Momentum flux of convective gravity
1047 waves derived from an offline gravity wave parameterization. Part II: Impacts on the Quasi-Biennial
1048 Oscillation, J. Atmos. Sci., 75, 3753–3775, https://doi.org/10.1175/JAS-D-18-0094.1, 2018.
1049 Kawatani, Y, Lee, J. N., and Hamilton, K.: Interannual variations of stratospheric water vapor in MLS
1050 observations and climate model simulations, J. Atmos. Sci., 71, 4072–4085,
1051 https://doi.org/10.1175/JAS-D-14-0164.1, 2014.
1052 Kawatani, Y., Hamilton, K., Sato, K., Dunkerton, T. J., Watanabe, S., and Kikuchi, K.: ENSO Modulation
1053 of the QBO: Results from MIROC Models with and without Nonorographic Gravity Wave
1054 Parameterization, J. Atmos. Sci., 76, 3893–3917, https://doi.org/10.1175/JAS-D-19-0163.1, 2019.
1055 Kelley, M., Schmidt, G. A., Nazarenko, L. S., Bauer, S. E., Ruedy, R., Russell, G. L., Ackerman, A. S.,
1056 Aleinov, I., Bauer, M., Bleck, R., Canuto, V., Cesana, G., Cheng, Y., Clune, T. L., Cook, B. I., Cruz,
1057 C. A., Del Genio, A. D., Elsaesser, G. S., Faluvegi, G., Kiang, N. Y., Kim, D., Lacis, A. A.,
1058 Leboissetier, A., LeGrande, A. N., Lo, K. K., Marshall, J., Matthews, E. E., McDermid, S., Mezuman,
1059 K., Miller, R. L., Murray, L. T., Oinas, V., Orbe, C., Pérez, C., García-Pando, C., Perlwitz, J. P.,
1060 Puma, M. J., Rind, D., Romanou, A., Shindell, D. T., Sun, S., Tausnev, N., Tsigaridis, K., Tselioudis,
1061 G., Weng, E., Wu, J., and Yao, M.-S.: GISS-E2.1: Configurations and climatology, J. Adv. Model.
1062 Earth Sy., 12, e2019MS002025, https://doi.org/10.1029/2019MS002025, 2020.

1063 Kumar V., Yoden, S., and Hitchman, M. H.: QBO and ENSO effects on the mean meridional circulation,
1064 polar vortex, subtropical westerly jets, and wave patterns during boreal winter, *J. Geophys. Res.* 127,
1065 e2022JD036691, https://doi.org/10.1029/2022JD036691, 2022.
1066 Labitzke, K.: On the interannual variability of the middle stratosphere during the northern winters, J.
1067 Meteorol. Soc. Jpn., 80, 963–971, http://doi.org/10.2151/jmsj1965.60.1_124, 1982.
1068 Liess, S. and Geller, M. A.: On the relationship between QBO and distribution of tropical deep
1069 convection, J. Geophys. Res., 117, D03108, http://dx.doi.org/10.1029/2011JD016317, 2012.
1070 Lindzen, R. S. and Holton, J. R.: A theory of the quasi-biennial oscillation, J. Atmos. Sci., 25, 1095–
1071 1107, https://doi.org/10.1175/1520-0469(1968)025%3C1095:ATOTQB%3E2.0.CO;2, 1968.
1072 Lott, F., Denvil, S., Butchart, N., Cagnazzo, C., Giorgetta, M. A., Hardiman, S. C., Manzini, E.,
1073 Krismer, T., Duvel, J.-P., Maury, P., Scinocca, J. F., Watanabe, S., and Yukimoto, S.: Kelvin
1074 and Rossby-gravity wave packets in the lower stratosphere of some high-top CMIP5 models, J.
1075 Geophys. Res., 119, 2156–2173, https://doi.org/10.1002/2013JD020797, 2014.
1076 Maruyama, T. and Tsuneoka, Y.: Anomalously short duration of the QBO at 50 hPa of the easterly wind
1077 phase in 1987 and its relationship to an El Niño event, J. Meteorol. Soc. Jpn., 66, 629–634,
1078 https://doi.org/10.2151/jmsj1965.66.4_629, 1988.
1079 Miller, R. L., Schmidt, G. A., Nazarenko, L. S., Bauer, S. E., Kelley, M., Ruedy, R., Russell, G. L.,
1080 Ackerman, A. S., Aleinov, I., Bauer, M., Bleck, R., Canuto, V., Cesana, G., Cheng, Y., Clune, T. L.,
1081 Cook, B. I., Cruz, C. A., Del Genio, A. D., Elsaesser, G. S., Faluvegi, G., Kiang, N. Y., Kim, D.,
1082 Lacis, A. A., Leboissetier, A., LeGrande, A. N., Lo, K. K., Marshall, J., Matthews, E. E., McDermid,
1083 S., Mezuman, K., Murray, L. T., Oinas, V., Orbe, C., Pérez García-Pando, C., Perlwitz, J. P., Puma,
1084 M. J., Rind, D., Romanou, A., Shindell, D. T., Sun, S., Tausnev, N., Tsigaridis, K., Tselioudis, G.,

1085 Weng, E., Wu, J., and Yao, M. S.: CMIP6 Historical Simulations (1850–2014) With GISS-E2.1, J.
1086 Adv. Model. Earth Syst., 13, e2019MS002034, https://doi.org/10.1029/2019MS002034, 2021.
1087 Moser, B. K. and Stevens, G. R.: Homogeneity of variance in the two-sample means test, Am. Stat., 46,
1088 19–21, https://doi.org/10.1080/00031305.1992.10475839, 1992.
1089 Naujokat, B.: An update of the observed quasi–biennial oscillation of the stratospheric winds over the
1090 tropics, J. Atmos. Sci., 43, 1873–1877, https://doi.org/10.1175/1520-
1091 0469(1986)043%3C1873:AUOTOQ%3E2.0.CO;2, 1986.
1092 Nazarenko, L. S., Tausnev, N., Russell, G. L., Rind, D., Miller, R. L., Schmidt, G. A., Bauer, S. E., Kelley,
1093 M., Ruedy, R., Ackerman, A. S., Aleinov, I., Bauer, M., Bleck, R., Canuto, V., Cesana, G., Cheng,
1094 Y., Clune, T. L., Cook, B. I., Cruz, C. A., Del Genio, A. D., Elsaesser, G. S., Faluvegi, G., Kiang, N.
1095 Y., Kim, D., Lacis, A. A., Leboissetier, A., LeGrande, A. N., Lo, K. K., Marshall, J., Matthews, E.
1096 E., McDermid, S., Mezuman, K., Murray, L. T., Oinas, V., Orbe, C., Pérez García-Pando, C.,
1097 Perlwitz, J. P., Puma, M. J., Romanou, A., Shindell, D. T., Sun, S., Tsigaridis, K., Tselioudis, G.,
1098 Weng, E., Wu, J., and Yao, M.-S.: Future Climate Change Under SSP Emission Scenarios With
1099 GISS-E2.1, J. Adv. Model. Earth Syst., 14,
1100 e2021MS002871, https://doi.org/10.1029/2021MS002871, 2022.
1101 Oort, A. H. and Yienger, J. J.: Observed interannual variability in the Hadley circulation and its
1102 connection to ENSO, J. Climate, 9, 2751–2767, https://doi.org/10.1175/1520-
1103 0442(1996)009<2751:Oivith>2.0.Co;2, 1996.
1104 Orbe, C., Rind, D., Jonas, J., Nazarenko, L., Faluvegi, G., Murray, L.T., Shindell, D.T., Tsigaridis, K.,
1105 Zhou, T., Kelley, M., and Schmidt, G.: GISS Model E2.2: A climate model optimized for the middle
1106 atmosphere. Part 2: Validation of large-scale transport and evaluation of climate response, *J.*
1107 *Geophys. Res. Atmos.*, 125, e2020JD033151, https://doi.org/10.1029/2020JD033151, 2020.

Philander, S. G. H.: El Niño, La Niña, and the Southern Oscillation, Academic Press, San Diego, 293pp., 1990.

Plumb, R. A.: The interaction of two internal waves with the mean flow: Implications for the theory of the quasi-biennial oscillation, J. Atmos. Sci., 34, 1847–1858, https://doi.org/10.1175/1520-0469(1977)034<1847:TIOTIW>2.0.CO;2, 1977.

Rao, J., Garfinkel, C. I., and White, I. P.: Impact of the Quasi-Biennial Oscillation on the Northern Winter Stratospheric Polar Vortex in CMIP5/6 Models, J. Climate, 33, 4787–4813, https://doi.org/10.1175/JCLI-D-19-0663.1, 2020a.

Rao, J., Garfinkel, C. I., and White, I. P.: Projected strengthening of the extratropical surface impacts of the stratospheric quasi-biennial oscillation, Geophys. Res. Lett., 47, e2020GL089149, https://doi.org/10.1029/2020GL089149, 2020b.

Rao, J., Garfinkel, C. I., and White, I. P.: Development of the Extratropical Response to the Stratospheric Quasi-Biennial Oscillation, J. Climate, 34, 7239–7255, https://doi.org/10.1175/JCLI-D-20-0960.1 2021.

Rao, J., Garfinkel, C. I., White, I. P., and Schwartz, C.: How does the Quasi-Biennial Oscillation affect the boreal winter tropospheric circulation in CMIP5/6 models?, J. Climate, 33, 8975–8996, https://doi.org/10.1175/JCLI-D-20-0024.1, 2020c.

Rayner, N. A., Parker, D. E., Horton, E. B., Folland, C. K., Alexander, L. V., Rowell, D. P., Kent, E. C., and Kaplan, A.: Global analyses of sea surface temperature, sea ice, and night marine air temperature since the late nineteenth century, J. Geophys. Res., 108, 4407, https://doi.org/10.1029/2002JD002670, 2003.

Richter, J. H., Solomon, A., and Bacmeister, J. T.: On the simulation of the quasi-biennial oscillation in the Community Atmosphere Model, version 5, J. Geophys. Res.-Atmos., 119, 3045–3062, https://doi.org/10.1002/2013JD021122, 2014.

Richter, J. H., Anstey, J. A., Butchart, N., Kawatani, Y., Meehl, G. A., Osprey, S., and Simpson, I. R.: Progress in simulating the quasi-biennial oscillation in CMIP models, J. Geophys. Res.-Atmos., 125, e2019JD032362, https://doi.org/10.1029/2019JD032362, 2020.

Rind, D., Lerner, J., Jonas, J., and McLinden, C.: Effects of resolution and model physics on tracer transports in the NASA Goddard Institute for Space Studies general circulation models, J. Geophys. Res., 112, D09315, https://doi.org/10.1029/2006JD007476, 2007.

Rind, D., Suozzo, R., Balachandran, N. K., Lacis, A., and Russell, G.: The GISS global climate-middle atmosphere model. Part I: Model structure and climatology, J. Atmos. Sci., 45, 329–370, https://doi.org/10.1175/1520-0469(1988)045%3C0329:TGGCMA%3E2.0.CO;2, 1988.

Rind, D., Jonas, J., Balachandran, N., Schmidt, G., and Lean, J.: The QBO in two GISS global climate models: 1. Generation of the QBO, J. Geophys. Res. Atmos., 119, 8798–8824, https://doi.org/10.1002/2014JD021678, 2014.

Rind, D., Orbe, C., Jonas, J., Nazarenko, L., Zhou, T., Kelley, M., Lacis, A., Shindell, D., Faluvegi, Russell, G., Bauer, M., Schmidt, G., Romanou, A., and Tausnev, N.: GISS Model E2.2: A climate model optimized for the middle atmosphere — Model structure, climatology, variability and climate sensitivity, J. Geophys. Res. Atmos., 125, e2019JD032204, https://doi.org/10.1029/2019JD032204, 2020.

Salby, M. L.: Physics of the Atmosphere and Climate, Cambridge University Press, New York, https://doi.org/10.1017/CBO9781139005265, 2012.

Salby, M. L. and Garcia, R. R.: Transient response to localized episodic heating in the tropics, Part 1: excitation and short-time near-field behavior, J. Atmos. Sci., 44, 458–498, https://doi.org/10.1175/1520-0469(1987)044%3C0458:TRTLEH%3E2.0.CO;2, 1987.

1154 Sarachik, E. S. and Cane, M. A.: The El Niño-Southern Oscillation Phenomenon, Cambridge University
1155 Press, Cambridge, 364pp., 2010.
1156 Scaife, A. A., Butchart, N., Warner, C. D., Stainforth, D., Norton, W., and Austin, J.: Realistic quasi-
1157 biennial oscillations in a simulation of the global climate, Geophys. Res. Lett., 27, 3481–3484,
1158 https://doi.org/10.1029/2000GL011625, 2000.
1159 Schirber, S., Manzini, E., Krismer, T. and Giorgetta, M.: The Quasi-Biennial Oscillation in a warmer
1160 climate: sensitivity to different gravity wave parameterizations, Climate Dynamics, 45, 825–
1161 836, https://doi.org/10.1007/s00382-014-2314-2, 2015.
1162 Schmidt, G. A., Kelley, M., Nazarenko, L., Ruedy, R., Russell, G. L., Aleinov, I., Bauer, M., Bauer, S.
1163 E., Bhat, M. K., Bleck, R., Canuto, V., Chen, Y.-H., Cheng, Y., Clune, T. L., Del Genio, A., de
1164 Fainchtein, R., Faluvegi, G., Hansen, J. E., Healy, R. J., Kiang, N. Y., Koch, D., Lacis, A. A.,
1165 LeGrande, A. N., Lerner, J., Lo, K. K., Matthews, E. E., Menon, S., Miller, R. L., Oinas, V.,
1166 Oloso, A. O., Perlwitz, J. P., Puma, M. J., Putman, W. M., Rind, D., Romanou, A., Sato, M.,
1167 Shindell, D. T., Sun, S., Syed, R. A., Tausnev, N., Tsigaridis, K., Unger, N., Voulgarakis, A.,
1168 Yao, M.-S., and Zhang, J.: Configuration and assessment of the GISS ModelE2 contributions to
1169 the CMIP5 archive, J. Adv. Model. Earth Syst., 6, 141–
1170 184, https://doi.org/10.1002/2013MS000265, 2014.
1171 Scott, R. K. and Haynes, P. H.: Internal interannual variability of the extratropical stratospheric
1172 circulation: The low-latitude flywheel, Q. J. Roy. Meteor. Soc., 124, 2149–
1173 2173, https://doi.org/10.1002/qj.49712455016, 1998.
1174 Serva, F., Cagnazzo, C., Christiansen, B., and Yang, S.: The influence of ENSO events on the
1175 stratospheric QBO in a multi-model ensemble, Climate Dynamics, 54, 2561–2575,
1176 https://doi.org/10.1007/s00382-020-05131-7, 2020.

Simpson, I. R., Shepherd, T. G., and Sigmond, M.: Dynamics of the lower stratospheric circulation response to ENSO, J. Atmos. Sci., 68, 2537–2556, https://doi.org/10.1175/JAS-D-11-05.1, 2011.

Sullivan, S. C., Schiro, K. A., Stubenrauch, C., and Gentine, P.: The response of tropical organized convection to El Niño warming, J. Geophys. Res.-Atmos., 124, 8481–8500, https://doi.org/10.1029/2019JD031026, 2019.

Taguchi, M.: Observed connection of the stratospheric quasi-biennial oscillation with El Niño–Southern Oscillation in radiosonde data, J. Geophys. Res., 115, D18120, https://doi.org/10.1029/2010JD014325, 2010.

Trepte, C. R. and Hitchman, M. H.: Tropical stratospheric circulation deduced from satellite aerosol data, Nature, 355, 626–628, https://doi.org/10.1038/355626a0, 1992.

Tsuda, T., Ratnam, M. V., Alexander, S. P., Kozu, T., and Takayabu, Y.: Temporal and spatial distributions of atmospheric wave energy in the equatorial stratosphere revealed by GPS radio occultation temperature data obtained with the CHAMP Satellite during 2001–2006, Earth Planets Space, 61, 525–533, https://doi.org/10.1186/BF03353169, 2009.

Wallace, J., Panetta, R., and Estberg, J.: Representation of the equatorial stratospheric quasi- biennial oscillation in EOF phase space, J. Atmos. Sci., 50, 1751–1762, https://doi.org/10.1175/1520-0469(1993)050<1751:ROTESQ>2.0.CO;2, 1993.

Watanabe, S., Kawatani, Y., Tomikawa, Y., Miyazaki, K., Takahashi, M., and Sato, K.: General aspects of a T213L256 middle atmosphere general circulation model, J. Geophys. Res.-Atmos., 113, D12110, https://doi.org/10.1029/2008JD010026, d12110, 2008.

Wang, C., Deser, C., Yu, J.-Y., DiNezio, P., and Clement, A.: El Niño–Southern Oscillation (ENSO): A review. In Reefs of the Eastern Pacific, Springer Sci. Publish., 85–106, https://doi.org/10.1007/978-94-017-7499-4_4, 2016.

1200 Xu, J.-S., On the relationship between the stratospheric quasi-biennial oscillation and the tropospheric
1201 southern oscillation, J. Atmos. Sci., 49, 725–734, https://doi.org/10.1175/1520-
1202 0469(1992)049<0725:OTRBTS>2.0.CO;2, 1992.
1203 Yoden, S., Kumar, V., Dhaka, S., and Hitchman, M.: Global monsoon systems and their modulation by
1204 the equatorial Quasi-Biennial Oscillation, MAUSAM, 74, 239–252,
1205 https://doi.org/10.54302/mausam.v74i2.5948, 2023.
1206 Yoo, C. and Son, S.-W.: Modulation of the boreal wintertime Madden-Julian oscillation by the
1207 stratospheric quasi-biennial oscillation, Geophys. Res. Lett., 43, 1392–1398,
1208 https://doi.org/10.1002%2F2016GL067762, 2016.
1209 Yu, J.-Y. and Mechoso, C. R.: A coupled atmosphere–ocean GCM study of the ENSO, J. Climate,
1210 14, 2329–2350, https://doi.org/10.1175/1520-0442(2001)014%3C2329:ACAOGS%3E2.0.CO;2,
1211 2001.
1212 Yuan, W., Geller, M. A., and Love, P. T.: ENSO influence on QBO modulations of the tropical
1213 tropopause, Q. J. Roy. Meteorol. Soc., 140, 1670–1676, https://doi.org/10.1002/qj.2247, 2014.
1214 Zawodny, J. M. and McCormick, M. P.: Stratospheric Aerosol and Gas Experiment II measurements of
1215 the quasi-biennial oscillations in ozone and nitrogen dioxide, J. Geophys. Res., 96, 9371– 9377,
1216 http://dx.doi.org/10.1029/91JD00517, 1991.
1217 Zhao, Y. and Sun, D.-Z.: ENSO asymmetry in CMIP6 models, J. Climate, 5555–5572,
1218 https://doi.org/10.1175/JCLI-D-21-0835.1, 2022.
1219 Zhang, C.: Large-scale variability of atmospheric deep convection in relation to sea surface temperature
1220 in the tropics, J. Climate, 6, 1898–1913, https://doi.org/10.1175/1520-
1221 0442(1993)006<1898:LSVOAD>2.0.CO;2, 1993.
1222

Table 1 The model configurations and respective ensemble simulations

Model configuration	Simulation	CMIP6 archive tag	Period	Ensemble size	Ensemble name
AMIP–OMA–SP	Historical AMIP	N/A	1850–2014	5	E1
AMIP–OMA–AP	Historical AMIP	N/A*	1850–2014	4	E2
Coupled–NINT–SP	CMIP6 Historical	N/A#	1850–2014	5	E3
Coupled–NINT–AP	CMIP6 Historical	E2-2-G.historical.r[1-5]i1p1f1	1850–2014	5	E4

*E2-2-G.amip.r[1-5]i1p3f1 in the CMIP6 archive are the outputs of the same model, but range from 1979 to 2014.

Coupled–NINT–SP outputs follow the CMIP6 protocol and naming. Four of five runs are available from NCCS portal at **https://portal.nccs.nasa.gov/datashare/giss_cmip6/CMIP/NASA-GISS/GISS-E2.2.1-G/**

1223

Table 2 The ENSO influence on the QBO period

Member		r1			r2			r3			r4			r5		
ENSO Phase		EL	LA	EL–LA	EL	LA	EL–LA	EL	LA	EL–LA	EL	LA	EL–LA	EL	LA	EL–LA
Period (month)	E1	31.1	34.0	***(–2.9)***	34.9	35.9	–1.0	29.4	32.9	–3.5	29.7	36.7	***(–7.0)***	30.5	35.7	***(–5.2)***
	E2	33.1	36.5	***(–3.4)***	31.5	35.6	***(–4.1)***	32.1	35.4	–3.2	29.4	36.8	***(–7.4)***	n/a	n/a	n/a
	E3	27.5	33.7	–6.2	28.0	30.5	–2.5	30.5	29.8	0.7	30.0	31.5	–1.5	28.2	32.0	–3.8
	E4	31.2	35.0	***(–3.8)***	29.8	32.4	***(–2.6)***	29.7	35.4	***(–5.7)***	28.0	34.7	***(–6.7)***	28.0	33.4	***(–5.4)***

E[1-4] denote the ensemble simulations AMIP-OMA-SP, AMIP-OMA-AP, Coupled-NINT-SP, and Coupled-NINT-AP, respectively. r[1-5] indicate the ensemble members of those simulations. EL and LA are short for El Niño than during La Niña, respectively. The numbers in parentheses denotes being statistically significantly different from zero at the 5% significance level.

1224

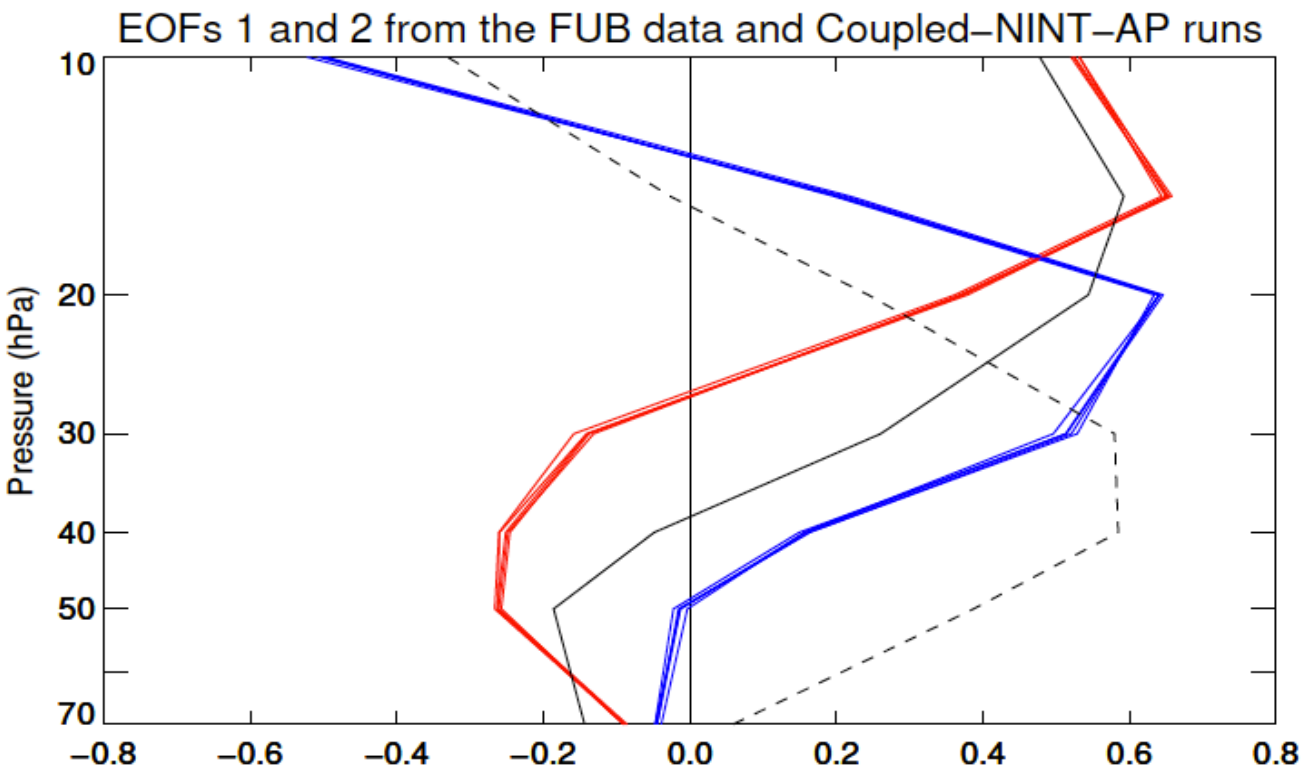

Fig. 1. Black lines depict the first (solid) and second (dashed) orthonormal eigenvectors derived from the monthly FUB zonal wind anomalies between 1953 and 2015. Colored lines delineate the first (red) and second (blue) orthonormal eigenvectors derived from the deseasonalized and smoothed equatorial zonal mean zonal winds between 1873 and 2013 from the five Coupled–NINT–AP runs.

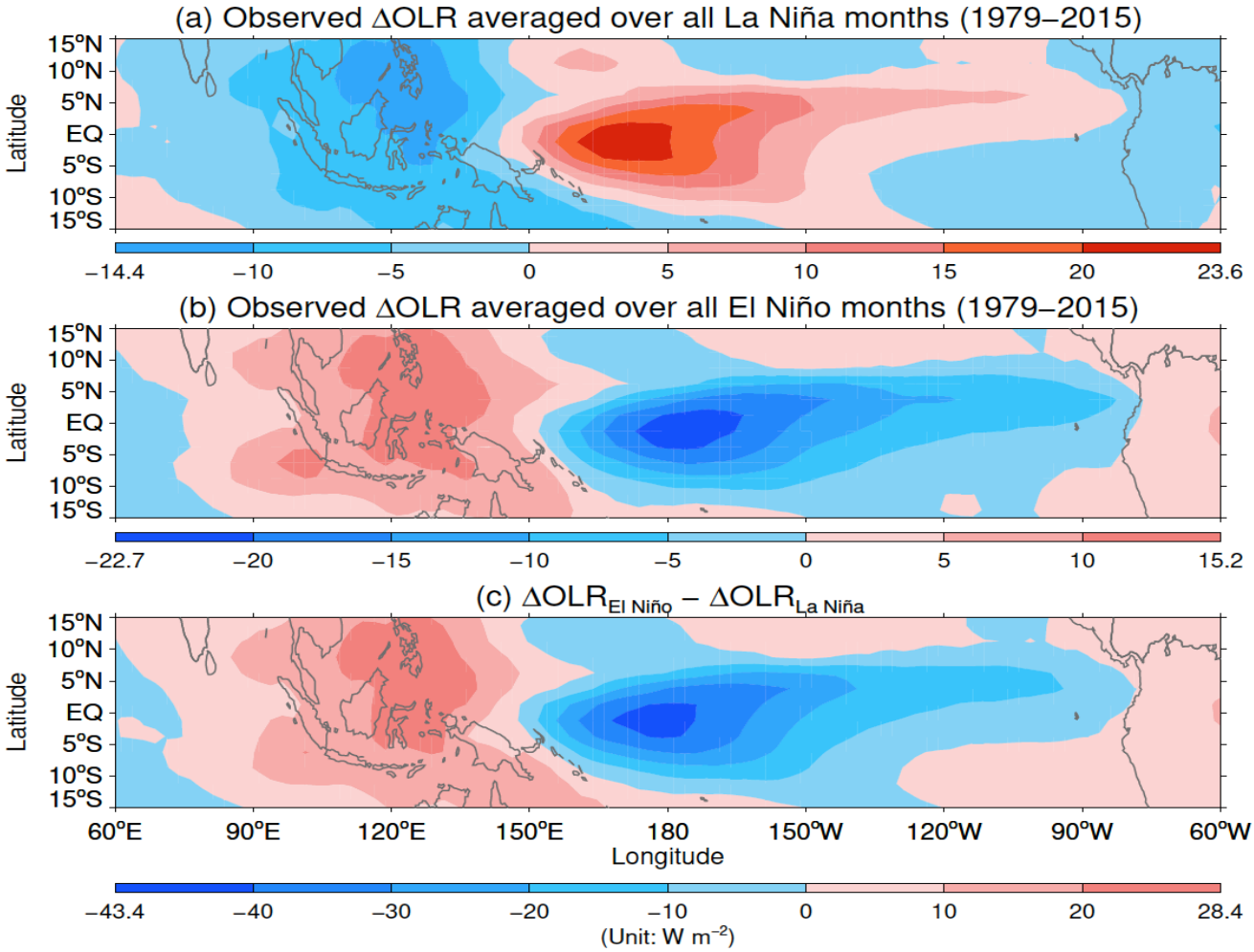

Fig. 2. Mean OLR deviations from climatology for (a) La Niña and (b) El Niño conditions over the tropical Indian and Pacific oceans. (c) Differences of mean OLR anomalies between El Niño and La Niña conditions. The mean composite OLR anomalies and their differences are derived from the datasets provided by NOAA NCEI.

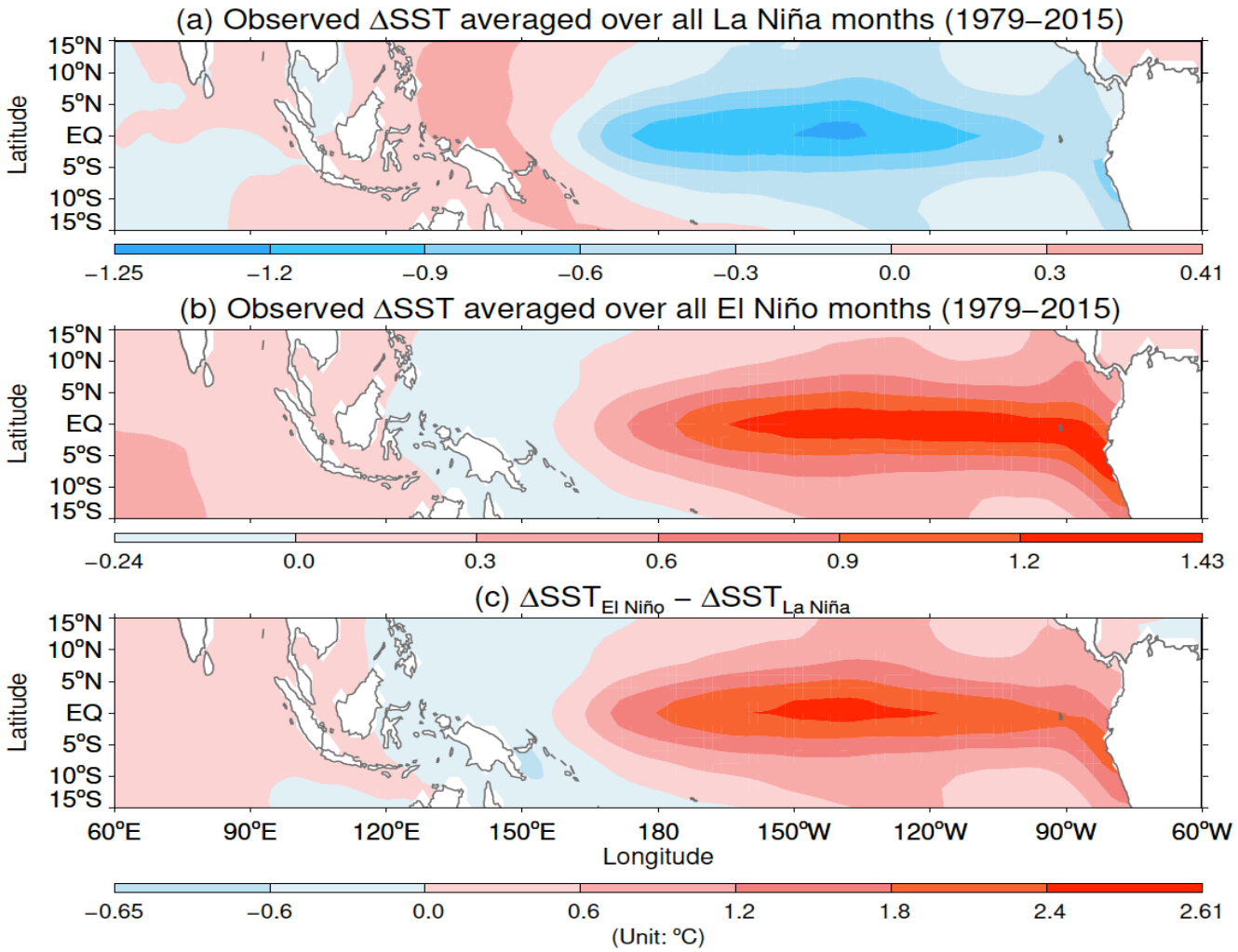

Fig. 3. Mean SST deviations from climatology for (a) La Niña and (b) El Niño conditions over the tropical Indian and Pacific oceans. (c) Differences of mean SST anomalies between El Niño and La Niña conditions. The mean composite SST anomalies and their differences are derived from the NOAA ERSSTv5 SST.

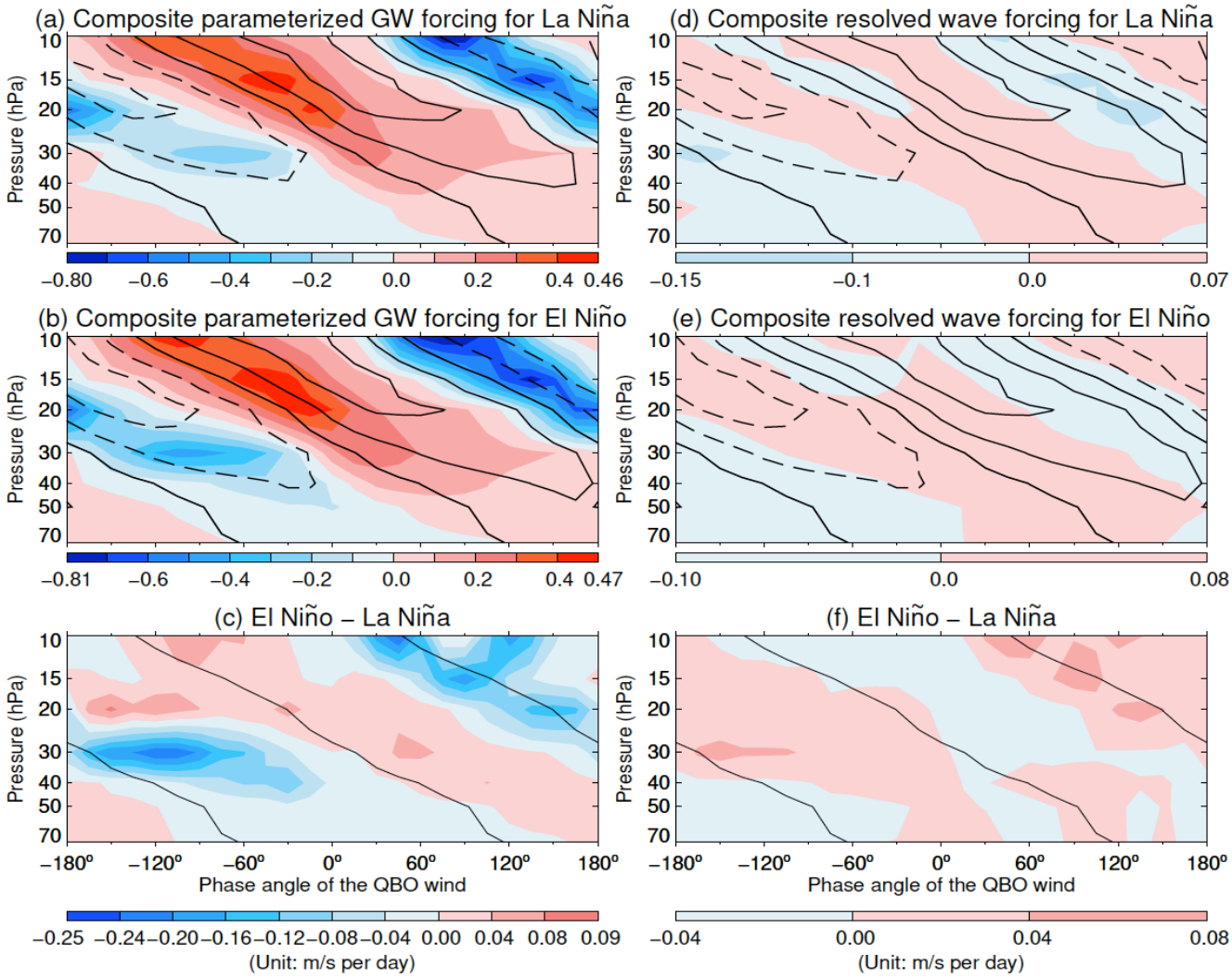

Fig. 4. Ensemble average of the composite QBO winds simulated by the Coupled–NINT–AP model during La Niña (upper panels) and El Niño (middle panels) is depicted by black contour lines where the contour interval is 10 m s^{-1} with dashed lines denoting negatives and solid lines denoting positives and zero. The location of strong shear zones of the QBO winds during ENSO extremes is delineated by the zero wind contour lines in lower panels. For color filled contours, left panels depict the ensemble average of the composite parameterized GW forcing simulated by the Coupled–NINT–AP model averaged from 5°S to 5°N during La Niña (a) and El Niño (b) and its composite difference between El Niño and La Niña (c); right panels depict the ensemble average of the composite resolved wave forcing simulated by the Coupled–NINT–AP model during La Niña (d) and El Niño (e) and its composite difference between El Niño and La Niña (f).

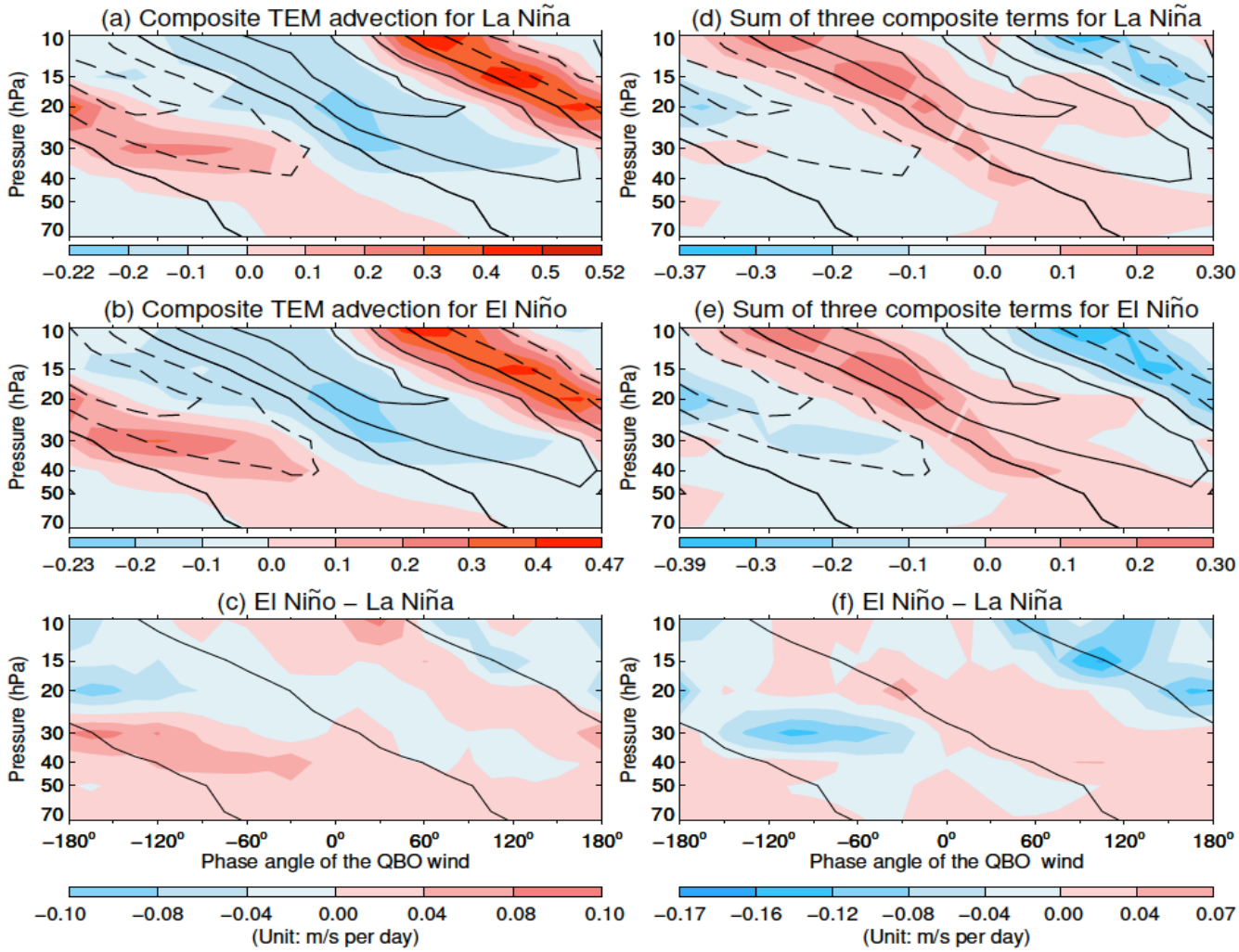

Fig. 5. The black contour lines are the same as those in Fig. 4. For color filled contours, left panels depict the ensemble average of the composite TEM advection simulated by the Coupled–NINT–AP model averaged from 5°S to 5°N during La Niña (a) and El Niño (b) and the composite difference between El Niño and La Niña (c); right panels depict the ensemble mean totaling of the composite fields of GW forcing, resolved wave forcing, and TEM advection simulated by the Coupled–NINT–AP model during La Niña (d) and El Niño (e) and the composite difference between El Niño and La Niña (f).

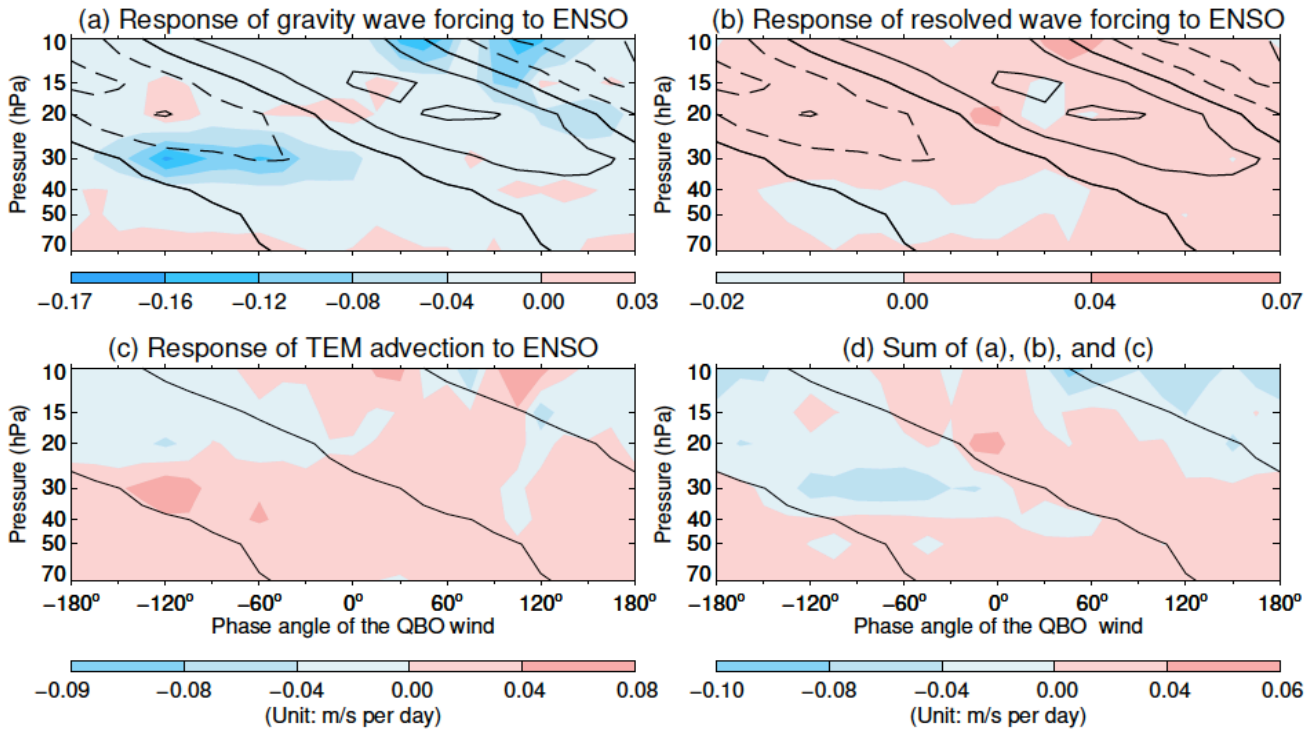

Fig. 6. (a) and (b) are the same as the bottom panels in Fig. 4 except for the Coupled–NINT–SP model. (c) and (d) are the same as the bottom panels in Fig. 5 except for the Coupled–NINT–SP model.

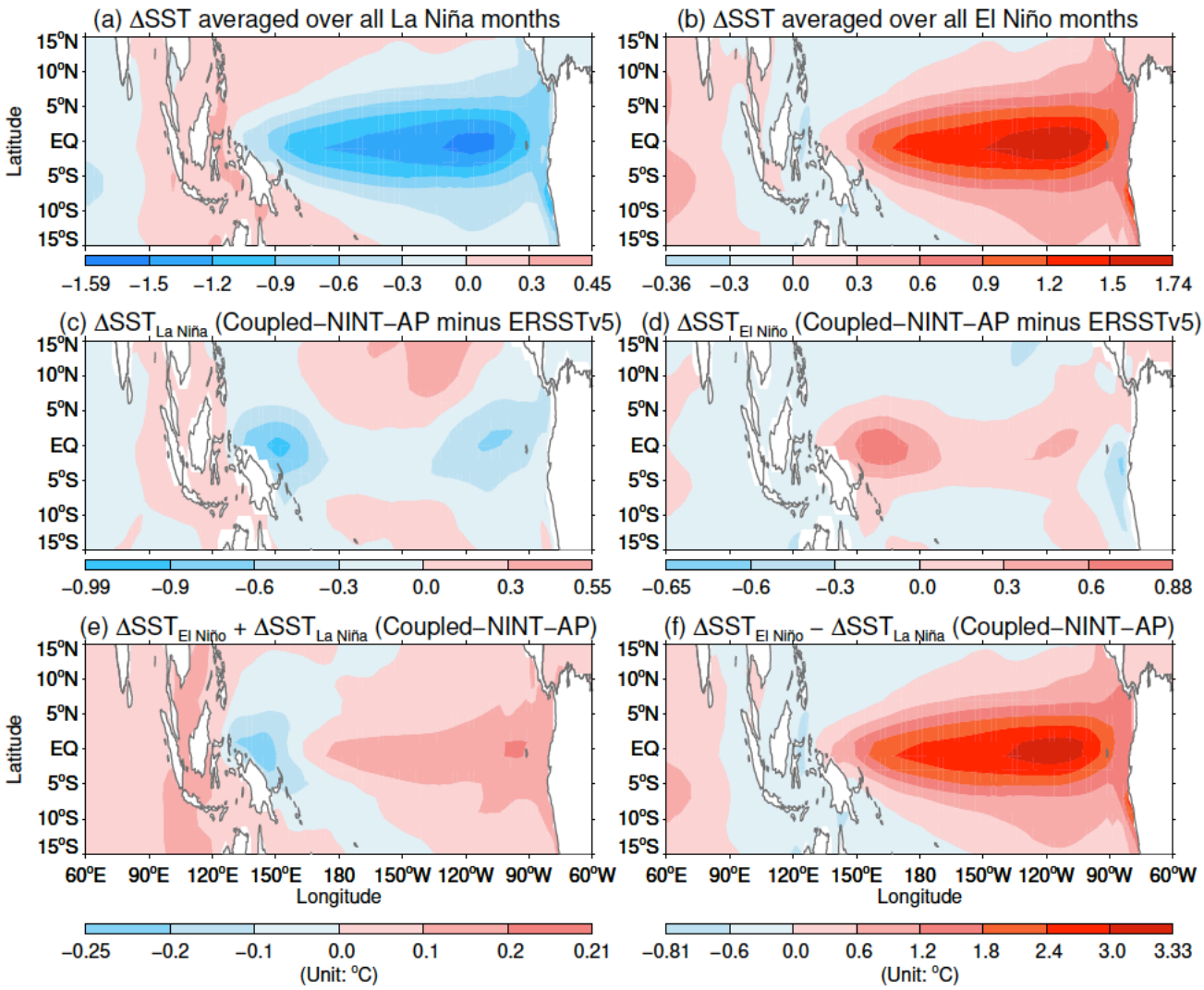

Fig. 7. Ensemble mean of the composite SST anomalies from the Coupled–NINT–AP runs averaged over all La Niña (a) and El Niño (b) months respectively over the 1871–2013 period. . Differences from observations are shown in (c) and (d). The sum and difference of model derived El Niño and La Niña SST anomalies are shown in (e) and (f), respectively.

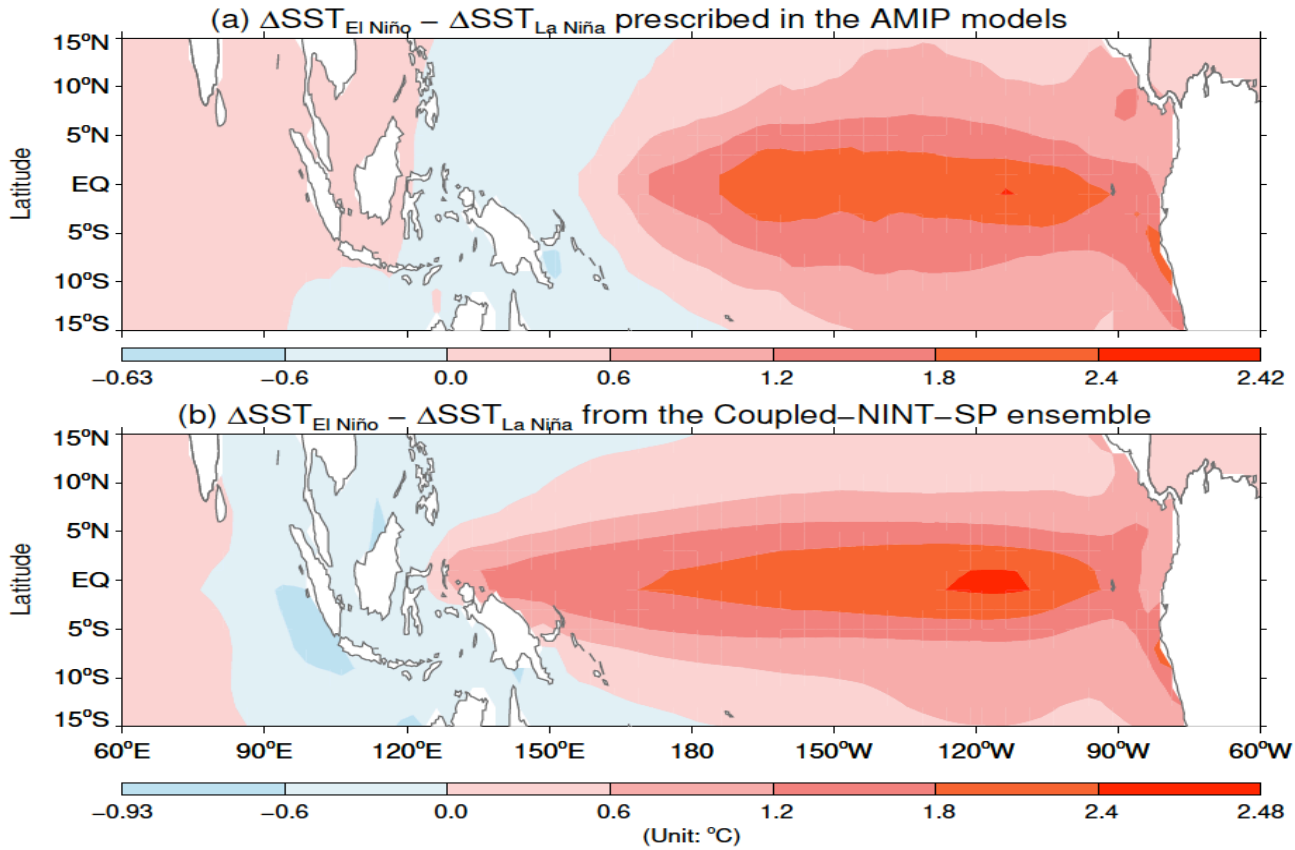

Fig. 8. Difference in the composite SST anomalies between El Niño and La Niña over the 1871–2013 period specified in the AMIP–OMA–SP and AMIP–OMA–AP models (a) and that simulated by the Coupled–NINT–SP model (b).

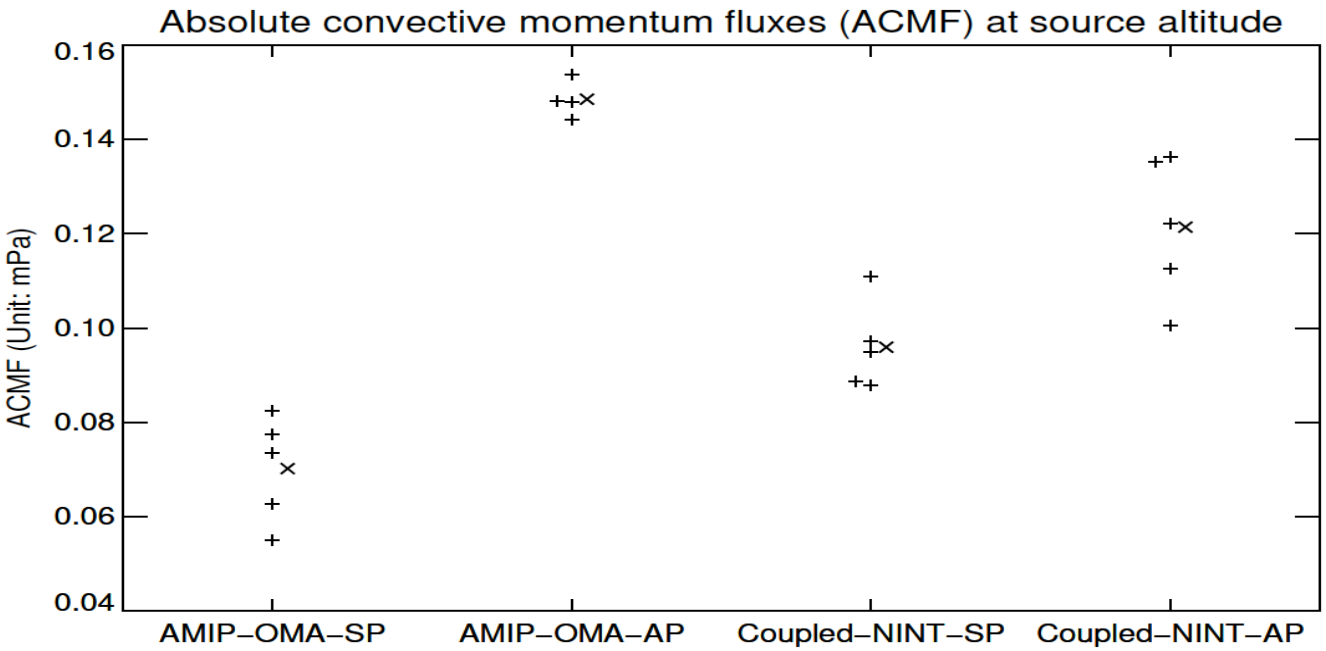

Fig. 9. Difference in the composite ACMF anomalies at the source altitude averaged over the 5°S – 5°N latitudinal belt between El Niño and La Niña over the 1871–2013 period. Plus symbol (+) denotes the difference from individual runs while cross symbol (×) represents each ensemble mean difference. Some symbols are slightly shifted leftward or rightward to avoid overlapping with other symbols.

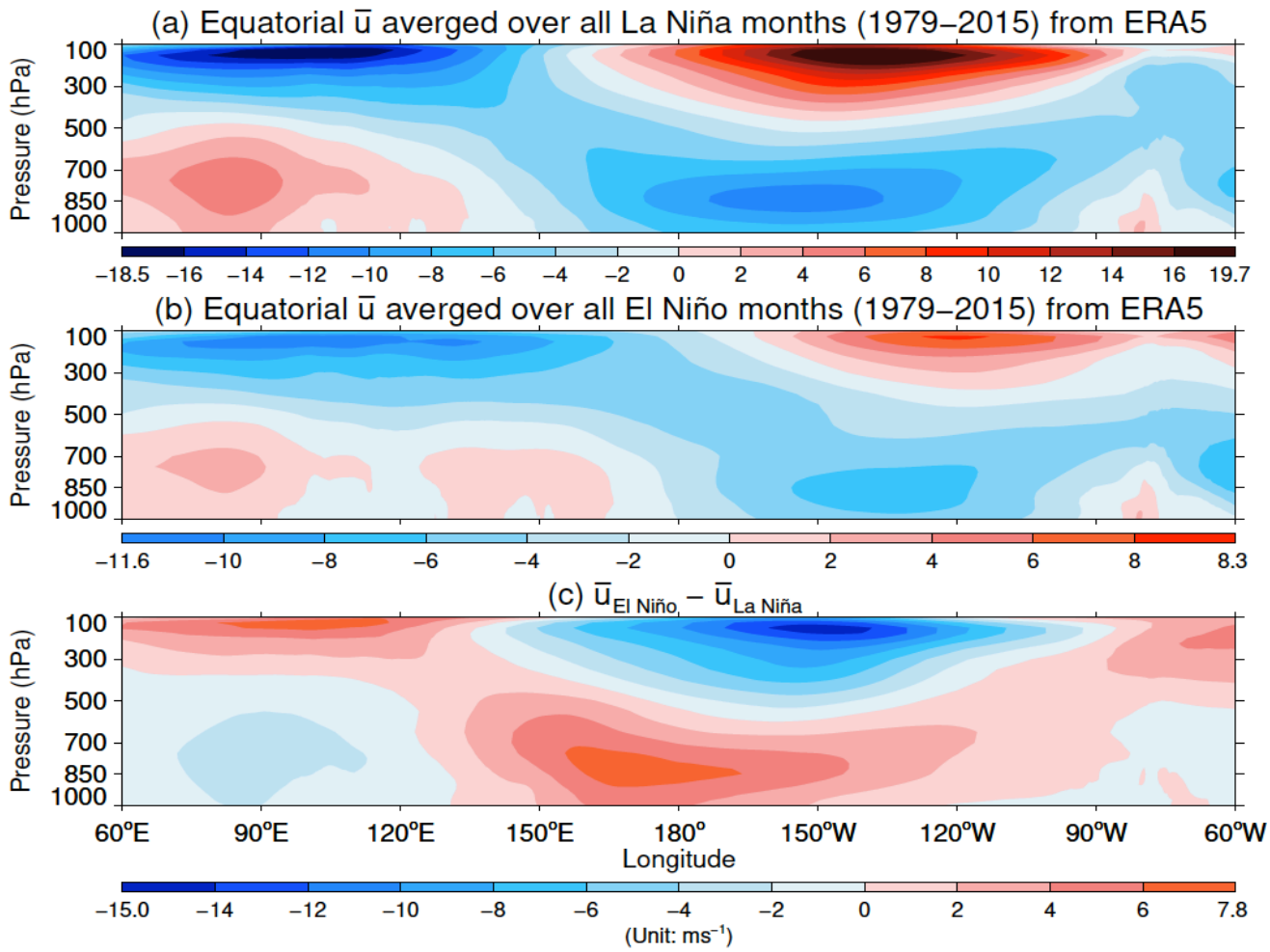

Fig. 10. Zonal winds from ERA5 averaged from 5°S to 5°N that are further averaged over all La Niña (a) and El Niño (b) months between 1979 and 2015 respectively, and their differences (c).

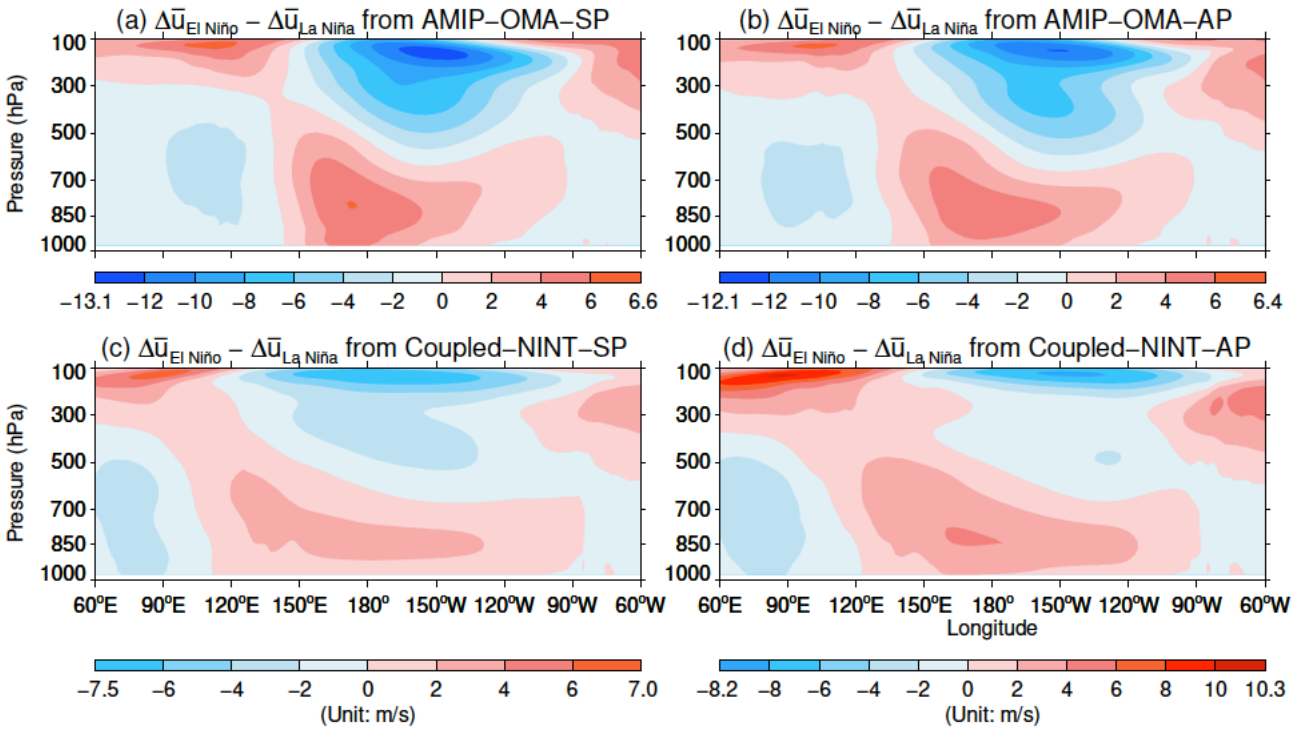

Fig. 11. Same as Fig. 10c but for the ensemble averages of the composite difference in zonal wind anomalies between El Niño and La Niña simulated by AMIP–OMA–SP (a), AMIP–OMA–AP (b), Coupled–NINT–SP (c), and Coupled–NINT–AP (d).

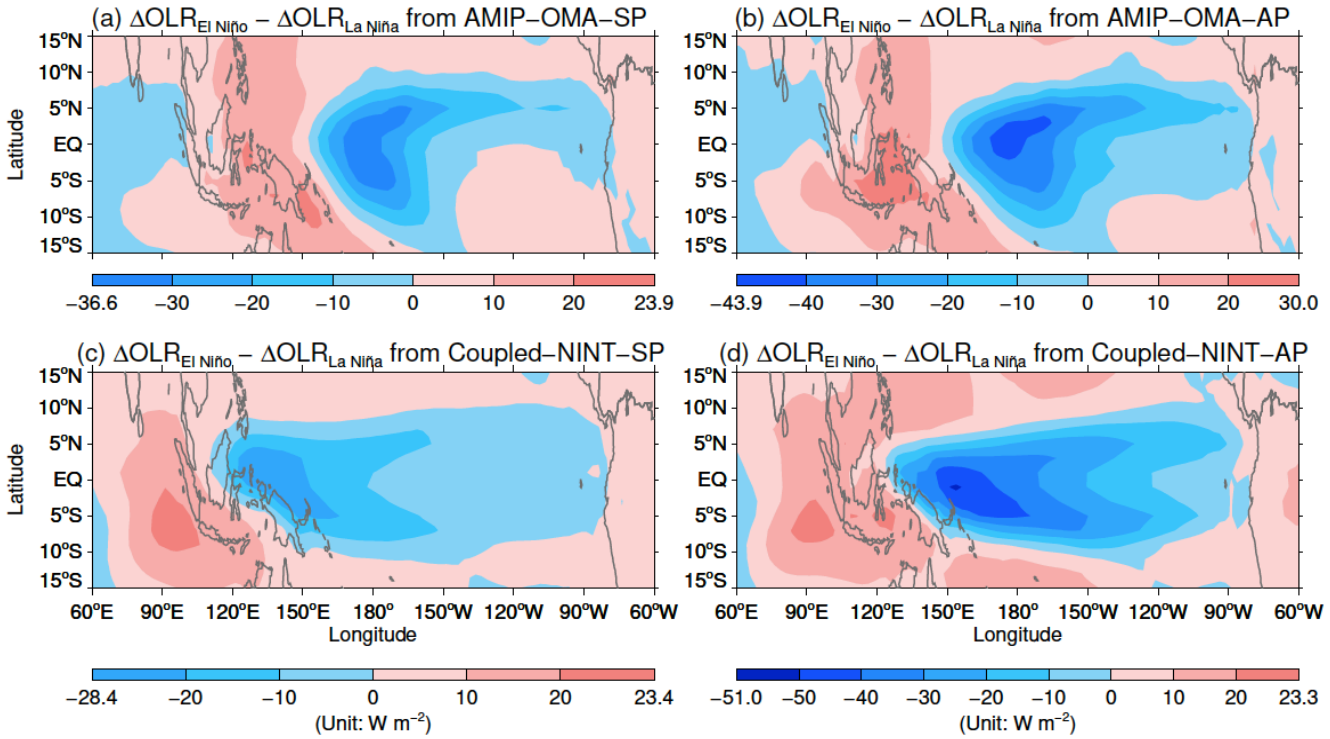

Fig. 12. Same as Fig. 11 but for the ensemble averages of the composite difference in OLR anomalies between El Niño and La Niña simulated by AMIP–OMA–SP (a), AMIP–OMA–AP (b), Coupled–NINT–SP (c), and Coupled–NINT–AP (d).

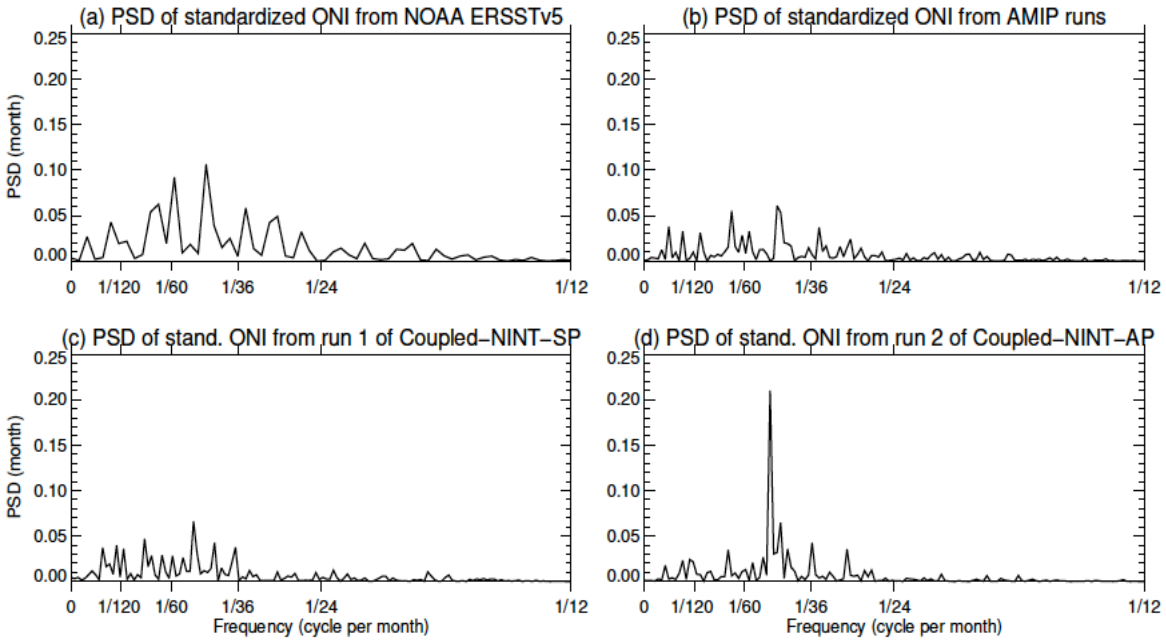

Fig. 13. Power spectral densities (PSD) of the standardized ONI between 1953 and 2015 derived from the NOAA ERSSTv5 SST (a), of standardized ONI between 1871 and 2013 derived from the HadISST1 dataset as used in the AMIP runs (b), of standardized ONIs between 1871 and 2013 simulated by the first realization of Coupled–NINT–SP (c) and the second realization of Coupled–NINT–AP (d), respectively.